Segmented Solid Surface Reflector Concentrically Stacked With Tubular Shape Memory Composite Hinges

Juan M. Fernandez[*], Andrew F. Paddock[†], Joshua E. Salazar[‡]
NASA Langley Research Center, Hampton, VA 23681, USA

and

Kevin S. O'Neal[§]
Analytical Mechanics Associates, Inc., NASA LaRC, VA 23681, USA

A new architecture for solid surface reflector antennas scalable to sizes greater than 10 m is presented. The design uses compact, light, and simple advanced deployable structures to create sub-reflectors that can be assembled in space into larger units using a robotic arm. The seven-panel hexagonal sub-reflector is divided into hexagonal panels that stack concentrically and vertically. The central panel is connected to each side panel on the back side by a pair of tubular shape memory composite hinges that enable the required deployment kinematics with controlled dynamics. A secondary mechanism closes the interpanel gap. The focus of the paper is on the development of the sub-reflector elements, namely the tubular hinges that use embedded heaters and sensors for triggering and control, the actuation mechanisms, and the lightweight sandwich construction reflector panels. A parametric study using finite element analyses was conducted to assess how design features of the hinge affect its stowage and deployment dynamics. The preliminary component fabrication and testing results for the two-panel assembly breadboard model are outlined. Finally, the results of the test campaign with the brassboard reflector model are presented. A comparison of deployed reflector surface deviation between the measured surface after the stowage and deployment process and the pre-test scans and the nominal surface revealed root mean square errors of less than 1 mm, as required by X-band radiofrequency transmission.

I. Introduction

Fixed solid surface reflector antennas are normally constructed up to a diameter of 4 m due to the size of launch vehicle fairings. Given their high surface accuracy and low transmission losses, they can target higher radio frequencies than deployable mesh or membrane reflectors, which are more scalable in nature. To increase volumetric packaging efficiency, several efforts have targeted deployable solid surface reflectors. However, in general, those designs have been limited in size to less than 10 m diameters due to high mass and mechanical complexity. The typical architecture is to have a central hub that is surrounded by a series of petals or gores supported on a deployable metering structure. The traditional approach is for these petals to be rigid, and thus such reflectors require a high degree of mechanical complexity to stow and deploy to the required accuracy, normally following a wrap-rib or radial and axial hinge approach for the backbone support structure [1]. Researchers have investigated advanced designs that make use

---

[*] Research Aerospace Engineer, Structural Dynamics Branch, NASA LaRC, 4 West Taylor Street, Mail Stop 230. AIAA Associate Fellow.

[†] Aerospace Engineer, Mechanical Systems Branch, NASA LaRC.

[‡] Research Aerospace Engineer, Structural Dynamics Branch, NASA LaRC.

[§] Aerospace Engineer, Structural and Thermal Systems Branch, NASA LaRC.

of deformable thin-shell composites reflective surfaces made from low-thermal expansion, high-strain carbon fiber composite materials that allow the entire reflector to stow more efficiently by elastically deforming the material [2-3]. Others have considered rigid reflective panels that are mechanically hinged to produce efficient packaging configurations that are constrained throughout deployment [1]. A promising new alternative approach uses high strain elastic rods to connect the panels allowing for greater flexibility in where segments can be stored in the spacecraft [5]. Advanced concepts that involve in-space assembly (ISA) [4], and spacecraft formation flying have been proposed to scale up the reflector surface [7]. Before the recent cancellation of the National Air and Space Administration (NASA) On-orbit Servicing, Assembly, and Manufacturing (OSAM-1) mission, Maxar Technologies had planned to demonstrate in-space assembly of a 3-m antenna reflector from seven 1-m size hexagonal rigid panels, which are fixed to one spacecraft facet [8]. Assembly of each side panel one by one to the central panel attached to the main spacecraft boom was to be carried out autonomously by a 5-m-long robotic arm that locates and bolts down each panel. The payload called Space Infrastructure Dexterous Robot (SPIDER) was to robotically assemble the communications antenna and demonstrate Ka-band radiofrequency (RF) transmission with a ground station on Earth.

A new collaboration effort was established in 2022 between NASA Langley Research Center (LaRC) and Maxar Technologies to study advanced packaging methods using flexible composite technology for the next generation of large, segmented, solid surface antenna reflectors compatible with in-space assembly by robotic arm operation. LaRC was tasked with developing an architecture and flexible composite substrate to simplify and reduce the number of robotic operations of scaled-up systems of SPIDER that would otherwise require multiple rings of hexagonal panels to enlarge the area of the aperture.

The down selected reflector architecture consists of sets of tubular composite hinges used to connect the backside of many rigid segments that form the parabolic reflector, which for a larger version will be assisted by the robotic arm. The construction of the tubular hinges and hexagonal panels is presented in this paper, as well as the component level analysis carried out on the hinges to characterize their quasi-static folding process and dynamic deployment behavior. The design of the two-panel (2/7th area) breadboard model demonstrator that was used to assess and validate the new concept will also be shown. This system is designed to serve as a 3.3-m scale sub-reflector for a future 10-m diameter robotically assembled reflector. The preliminary validation test campaign, followed by requirements compliance and concept feasibility assessment was completed in 2023. A subsequent effort using internal LaRC funding was initiated in 2024 for the development of a brassboard reflector model to be used for field testing and incorporating the approximate layout and functionality of the finished design. The preliminary results of this on-going final validation test campaign are presented before moving to production.

II. Architecture Design

The use of a new shape memory composite (SMC) material with integrated heating and sensing capabilities was developed to reduce part count, complexity, power requirements, and cost of larger antenna reflectors, while enabling a high deployed stiffness solution with predictable and controlled deployment dynamics [8]. The deployable reflector uses these SMC hinges to connect and stack all hexagonal rigid panels stowed in a cup down configuration under the central cup up panel, as shown in Fig. 1 [9]. The initial concept produced a vertically staggered panel assembly configuration such that the SMC hinge would seamlessly mate the side panels with the central panel, without the need of a secondary closing mechanism [10]. However, for a volumetrically efficient stowed configuration, where all side panels are stacked concentrically under the central one, a secondary spring-loaded mechanism is used to close the initial panel-to-panel gap left by the deployment of the composite hinges. Each pair of SMC hinges are anchored to each side panel by a carriage that translates along two side tracks or rails parallel to the hinge longitudinal axis. A mechanical reel that has a lanyard connected to a constant force spring provides the actuation force and necessary extension to close the inter-panel gap. A hold down mechanism in the form of a Frangibolt from TiNi Aerospace[**] secures the assembly for launch and until the pair of tubular SMC hinges have completed the initial rotation of the side panel, as shown in Fig. 2.

The outermost side panel (furthest from the central one) will connect to the spacecraft boom. As this panel deploys first, the stacked sub-reflector will be displaced from the spacecraft and the rest of the side panels will deploy one at time triggered by the thermally actuated SMC hinges. The final product is a series of high-precision sub-reflectors, each cantilevered from a small offset boom that the robotic arm will use to place and fix to the main central deployable sub-reflector already supported from the main spacecraft boom, as shown in Fig. 3. To increase the number of load paths through each sub-reflector and increase global deployed stiffness, the same type of

---

[**] Specific vendor and manufacturer names are explicitly mentioned only to accurately describe the analytical tools used. The use of vendor and manufacturer names does not imply an endorsement by NASA nor does it imply that the specified equipment is the best available.

Interconnect Assembly Plates used in the SPIDER demonstration is envisioned to secure additional side panels from the central and side sub-reflectors. The goal is to enable an architecture that does not require a robotic arm longer than the size of the central sub-reflector in order to keep cost down as the system scales up since the robotic arm is one of the main cost drivers.

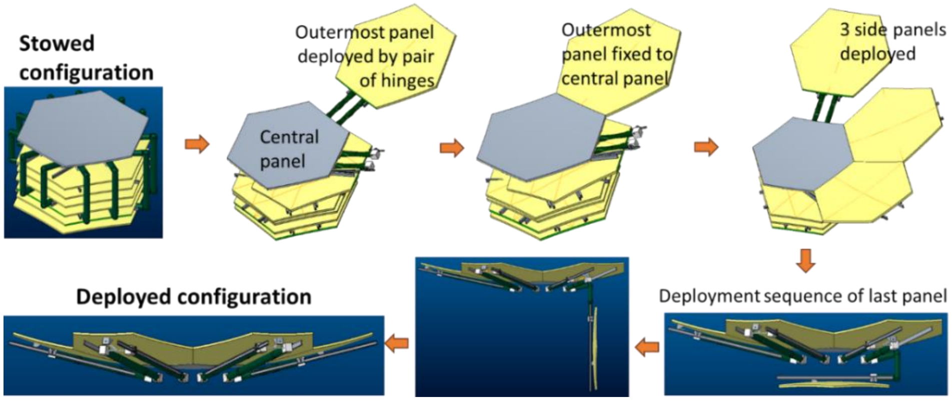

Fig. 1. Deployment sequence of a concentrically stacked seven-panel reflector by SMC hinges. Side panel deployment occurs one at a time from the outmost panel until all are fixed to the central panel

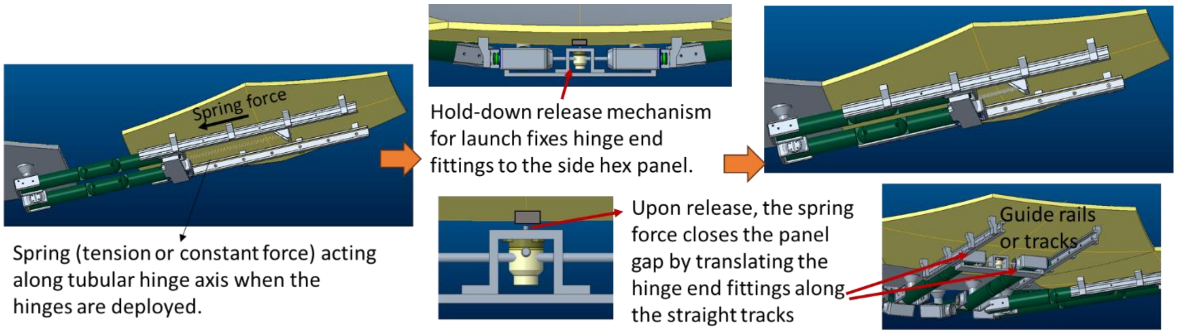

Fig. 2. Secondary spring-loaded mechanism to close the initial inter-panel gap left by the pair of hinges.

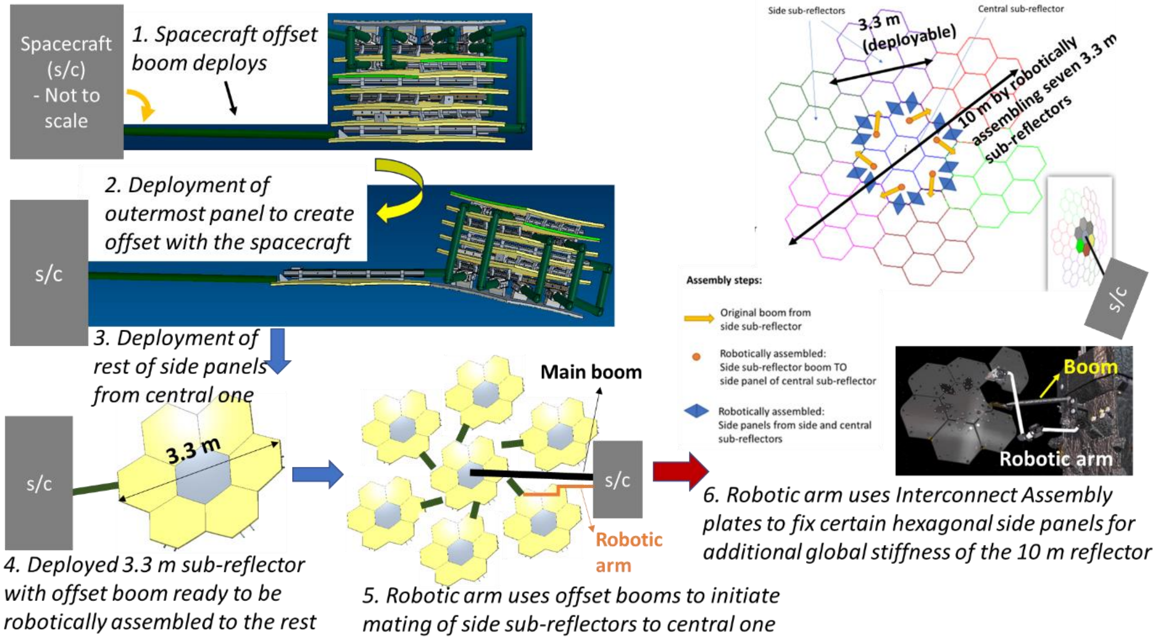

Fig. 3. Scalable architecture design using a combination of deployable and robotic arm in-space assembly. The figure shows the steps to construct a 10-m-class reflector.

III. Tubular Hinge Design and Analysis

The key technology that enables compact stowage of the numerous rigid panels in a concentrically stacked configuration is the composite tubular hinge. Before the SMC version was developed, the tubular hinge was initially conceived as being made from passive carbon fiber reinforced plastic (CFRP) material. In the current design, the side panel is cantilevered from the central panel by a pair of hinges, and thus this deformable backbone structure needs to provide the dimensional and structural stability required for a precision reflector, as well as the flexibility to change the configuration of the system from packaged to deployed. Since the vertical offset of each side panel from the central one is different in the stack, every pair of hinges has a unique geometry, as represented in the top image of Fig. 3. The hinges are composite tubes with a pair of diametrically opposite dogbone-shaped cutouts that enable localized pinching and folding of the hinge without damage [11]. Dogbone slots are used to increase deployed stiffness and minimize the risk of hinge snap back and a deployment anomaly [12] compared with straight slots with a constant slot width. The innermost panel in the stack will have a single pair of dogbone slots as the vertical offset from the neighboring central panel is small. The rest of the five side panels will all have two pairs of dogbone slots separated a certain distance proportional to the vertical offset from the central panel they need to clear in the stacked state. Two different designs of single-slot hinge pairs for Side Panel #1 in the stack are shown in Fig. 4 (a). These SMC hinges have integrated heaters for thermal actuation. The heater leads can be observed protruding from one of the hinge ends. A longer two-slot hinge for Side Panel #2 is presented in Fig. 4 (b). Since the vertical offset of each unique hinge pair depends on the system level design of the reflector with factors such as minimum panel thickness, panel area, or secondary closing mechanism design, that were subject to change, it was necessary to understand the design space for the tubular hinges given a set of building-block features common in all designs.

A parametric study for a single-slot hinge was first produced assuming a traditional thin-ply CFRP laminate to assess how design features affected three critical performance metrics that allowed down-selection:

1) Composite laminate strains in the folded state of the hinge.
2) The deployment moment-rotation relationship to determined steady-state and peak deployment moment to overcome snap back, as well as hinge deployed stiffness.
3) Whether the hinge snaps back at the end of deployment with an inertial tip mass equivalent to the side panel assembly attached. The tubular hinge stiffness drives both the dynamic peak moment and the locking moment that must be applied to fold the hinge.

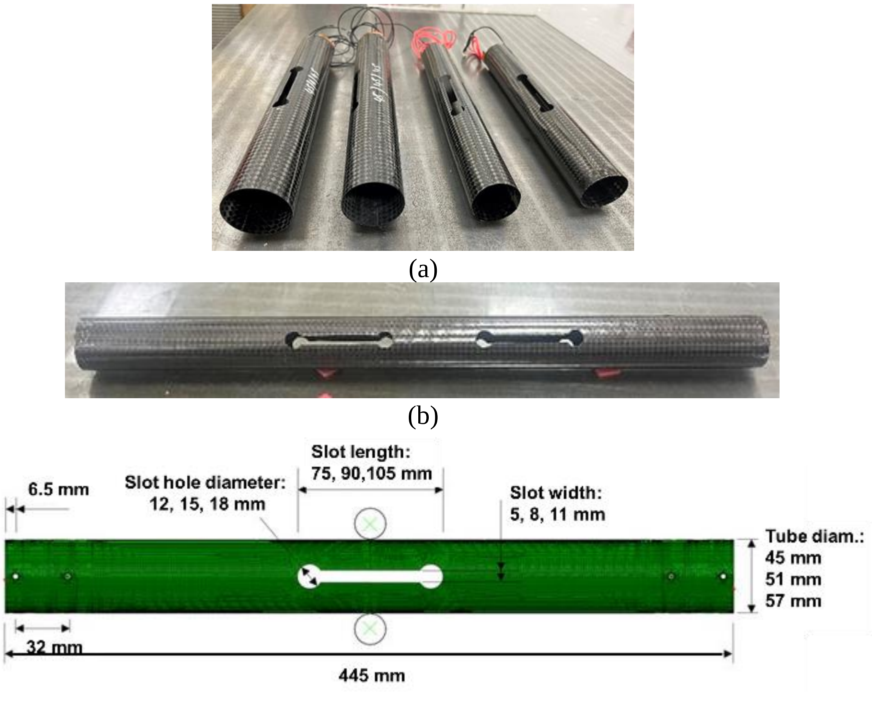

(c)

Fig. 4. Shape memory composite hinges with integrated heaters and the same dogbone slot geometry: (a) single-slot hinge pairs with a tube diameter of 45 mm (left) and 38 mm (right); (b) two-slot hinge with a tube diameter of 45 mm. (c) Design geometric parameters used in the trade study of the single-slot tubular hinge.

Three independent geometric parameters were traded in the study: tube diameter, hinge slot length, and the diameter at the end of the dogbone slot (with the slot width being proportional to it). Three different dimensions (small, medium and large) for the three independent parameters were used, as shown in Fig. 4 (c). The hinge parametric study generated a total of 27 unique design cases for analysis.

The finite element analysis (FEA) software Abaqus was used to simulate the quasi-static folding and deployment of the simple tubular hinge. The hinge composite laminate consisted of a three-ply [45PW/0PW/45PW] layup, with the outer plies having a plain weave fabric with fibers oriented at ±45° and the inner ply having a plain weave with fibers oriented in the 0° and 90° orientations relatives to the hinge longitudinal axis. A thin-ply composite material consisting of an intermediate modulus M30S carbon fiber with a PMT-F7 toughened epoxy matrix was assumed. The ply thickness was 0.06 mm. The composite laminate properties were: Young's modulus of 48.6 GPa in the axial and transverse direction, shear modulus of 29.7 GPa, Poisson's ratio of 0.46, and density of 1,520 kg/m^3.

One critical design parameter that affects the hinge response is how the hinge interfaces with the two panels it connects to. Tubular hinges with various end conditions were first analyzed to assess hinge stiffness, deployment moment-rotation behavior, and folding strains. These hinges all had a 45-mm diameter, 90-mm slot length, 15-mm slot hole diameter, and 8-mm slot width. This hinge design is considered the nominal case and was used for initial manufacturing trials. The hinge ends were either: a) completely free; b) restrained partially by a pair of soft springs that connect sections diametrically-opposite; c) completely restrained to the initial circular shape by internal plugs; d) or by two pairs of pins/rods that connect sections diametrically opposite, as shown in Fig. 5. The bending test fixture presented in Fig. 5 was used to measure the quasi-static deployment moment-rotation relationship of these hinges for correlation with the FEA. Motors driving the hinge ends from folded to deployed using a gear and lead screw rotate the ends in steps by equal amounts while the torque sensors in line with the rotation axis measured the self-deployment moment of the hinge. Different hinge end conditions were investigated using this bending test fixture.

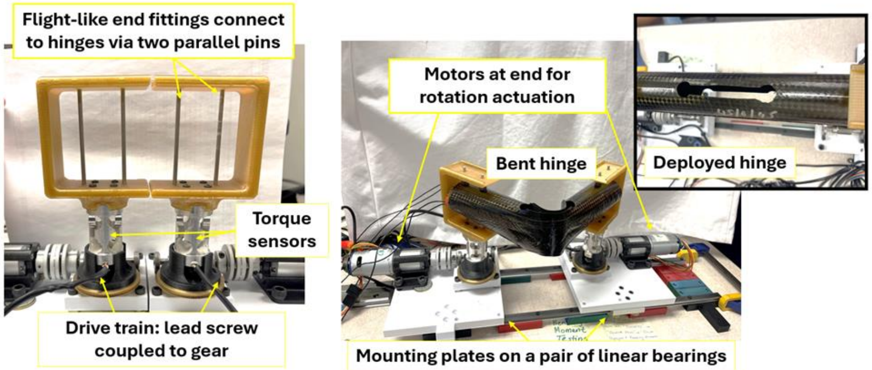

Fig. 5. Bending test fixture with representative hinge-end boundary conditions for moment-rotation measurement.

The analyses determined that the plugged-end condition was too stiff to allow this design to fold beyond a total 135º hinge rotation, producing high folding strains and a high peak moment 230% larger than the other cases. The case with the free ends showed the lowest folding strains, as the ends could ovalized completely, but produced the lowest deployed stiffness. The soft-spring and parallel-rod fittings partially constrained the ends and presented a compromise between folding strains and deployed stiffness and had similar peak moments as the free-ends case. It was decided to use the two parallel pins option as a simpler approach to implement physically, so all subsequent simulations, including the parametric study, used these boundary conditions.

For the parametric study of the single-slot hinge, the quasi-static folding was carried out by first pinching the slots together using two 25-mm diameter mandrels. Then, opposing rotations to the ends were prescribed to begin folding the pinched hinge. The two mandrels were removed when the hinge were partially folded, and the analysis continued until the tube ends met with the hinge fully folded at about 175º. The strain field in the stowed state were recorded. The maximum principal strains in the folded condition of all 27 hinge design cases simulated are presented in Fig. 6. The peak compressive strains are normally located near the center of the circular end holes of the dogbone slots at the interior shell ligament of the folded region. Several conclusions can be drawn from this graph. First, it is surprising to find that for cases other than for the smallest slot length of 75 mm, the growth in the diameter of the hole is proportional to the maximum compressive strain. Removing more material at the ends of the slot is only effective if it impacts the arc length needed to fold the tube. Second, folded strains diminish with both the tube diameter size and the slot length. Finally, folded strains between 1.2% to 2.2% are expected, suggesting the use of intermediate modulus carbon fiber laminates with high strain to failure.

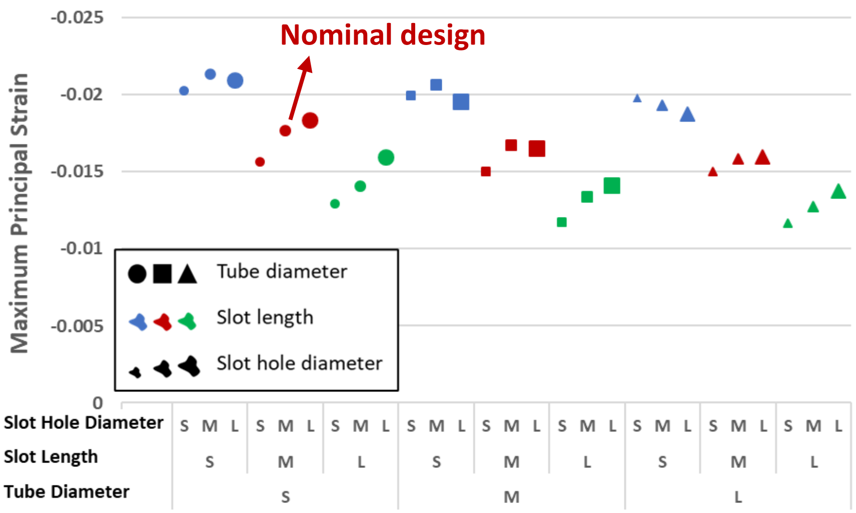

Fig. 6. Maximum principal strains obtained in the folded state of the hinge for all 27 design cases from combining the three independent design parameters (tube diameter, slot length, and slot hole diameter) at the different sizes: small (S), medium (M), and large (L). The nominal hinge design adopted is also highlighted.

For the deployment phase, two types of analyses were carried out. First, a quasi-static deployment step by prescribing equal rotations on both ends of the tube was performed until the hinge started to snap through. Then the quasi-static simulation was completed using a dynamic solver until the hinge fully straightened out. This approach provided the type of controlled deployment moment-rotation graph shown in Fig. 7 that was physically implemented in the bending test fixture shown in Fig. 5.

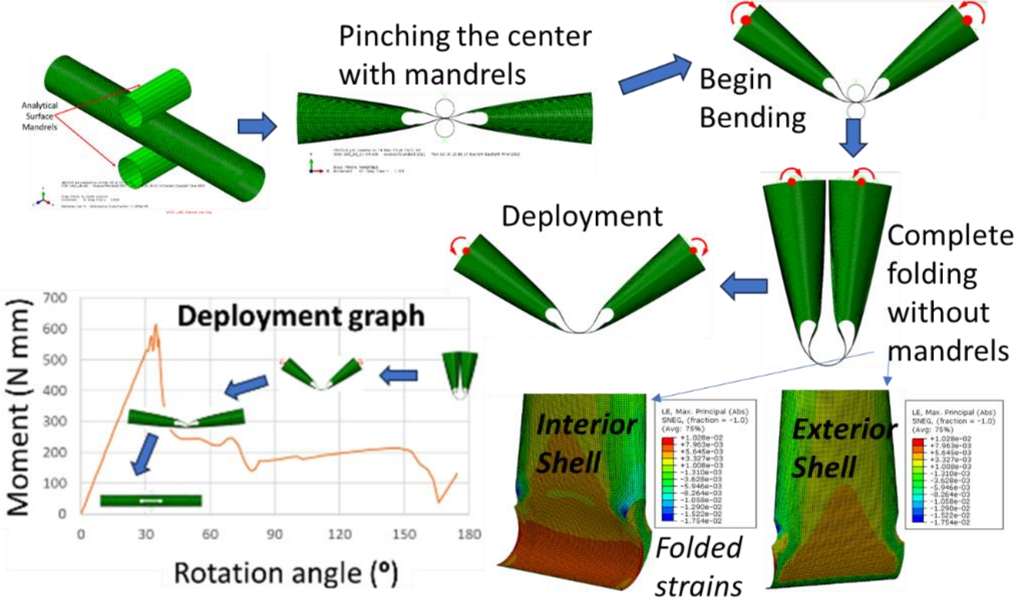

Fig. 7. Analysis steps to quasi-statically fold and deploy the single-slot hinge. The folded hinge strains in the interior and exterior shells around the slots are shown, as well as the deployment moment-rotation graph with a 200 N-mm near-constant characteristic steady-state moment until snap-through at a 600 N-mm peak moment at a remaining 35º rotation angle.

The second analysis approach was an implicit dynamic deployment simulation, where at one end of the hinge the same boundary conditions and local deformation of the end of the quasi-static folded state were kept fixed, while at the opposite end the constraint on the rotation axis was released. Mass proportional viscous damping was used in the analysis. The goal of this dynamic case was to assess if the hinge snapped back to the straight configuration or not. Three of the hinge designs analysed did not achieve a complete deployment. These cases all had the large size tube diameter of 57 mm combined with the small size slot diameter hole of 12 mm and slot width of 5 mm. The slot length size did not make a difference. The inside of the folded tube did not recover fully during deployment and forced the hinge to either backlash or snap back, as shown in the rightmost image of Fig. 8 (a). It is believed that for the smaller diameter tubes with the larger slots the shell ligaments near the slots subtend a smaller arc length and thus are more flexible. The three cases that did not finish straight stowed/released more strain energy than the ones with larger slots. The base moment-rotation graph for the nominal case is shown in Fig. 8 (b). Three moment peaks of increasing magnitude before the hinge fully snaps through are visible. The first peak at a 90º rotation angle is minor and corresponds to the folded ligaments slightly traveling axially and rearranging their configuration. The second peak at a 30º remaining angle corresponds to snap-though of the outer ligament. The third peak, which is the most energetic one, at a 6º angle corresponds to the snap-through of the inner ligament. After the hinge recovers its straight configuration, the tube continues to vibrate back and forth about the 0º angle producing very high moments of 7 Nm – 10 Nm at the base until the kinetic energy dissipates. The dynamic deployment sequence of a hinge with the nominal design dimensions is shown in the inset of Fig. 8 (b).

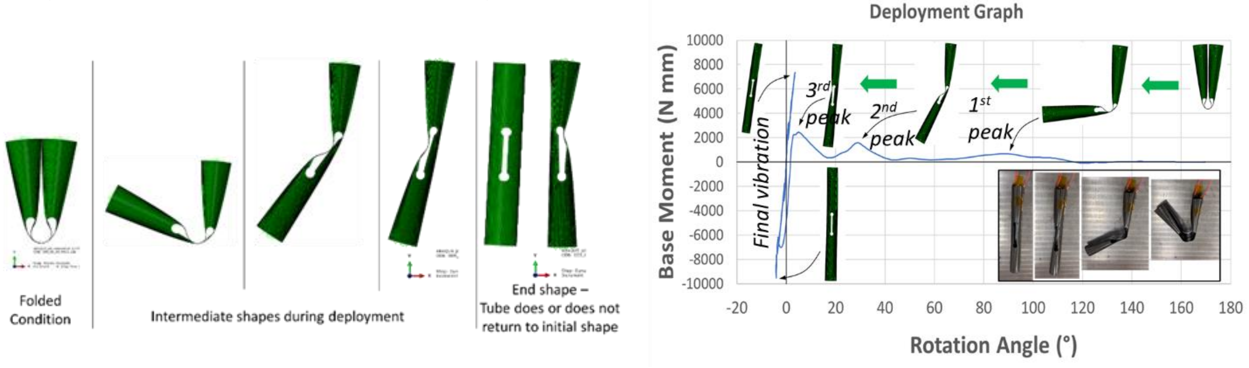

(a) (b)

Fig. 8. Dynamic deployment steps of the hinge without a tip mass attached to the moving end. (a) The simulated end shapes on the right show two different cases: one where the tube has returned to the straight configuration, and one where the tube has snapped-back into an unwanted end state; (b) deployment moment-rotation relationship graph showing final moment peaks when the hinge snaps through. Also shown in the inset the test article deployed using the embedded heaters and locking into the final straight configuration.

In parallel to the hinge design, a material development effort produced a new shape memory polymer to be adopted as the composite matrix for the advanced design of the tubular hinge. A mechanical properties study on plain weave SMC laminates determined that the hinge thin-shell material when bent uniformly above its glass transition temperature (Tg) of 125 ºC could experience tow microbuckling and kinking at a folding radius less than 20 mm. In general, this led to some intraply and interply delamination in the compression side of the kinked region. However, the deformation did not lead to loss of shape recovery unless tow/fiber/resin fracture was also present, which was experimentally determined to onset at a folding radius less than 6 mm. For the 0.18-mm wall thickness of the hinge laminate, this results in a not-to-exceed surface compression strain of 1.50%. For reference, the nominal hinge design with a traditional stiff epoxy matrix shows a maximum folded strain level of 1.78%, as reported in Fig. 7. However, the deformation and strain field on a SMC hinge design folded above its Tg is expected to be different. In fact, no damage has been visually observed on the SMC hinge specimens tested, though it is believed that the slot design may be marginal against failure. A longer slot length would reduce the compressive strain levels around the slot end and could be considered in a future design iteration to increase failure margin.

The next step in the analysis process involved the assessment of the folding and deployment behavior of a two-slot hinge. A FEA of the quasi-static folding of a single hinge from Side Panel #2 is presented in Fig. 9. Achieving a folded state that matched the desired end configuration needed in the panel stack, which results in a rotation angle of 92º for one end and 100º for the other end, required multiple analysis steps. First, effectively pinching the two slots required two pairs of mandrels moving synchronously. Then, the two lines of nodes between mandrels were pinned while the mandrels were moved out. Using several cycles of partial rotation between the left and right side of the hinge while one set of nodes was pinned, and the other set was released was necessary to complete the rotation of the hinge ends into the desired relative angles. The dynamic deployment study under this configuration is ongoing.

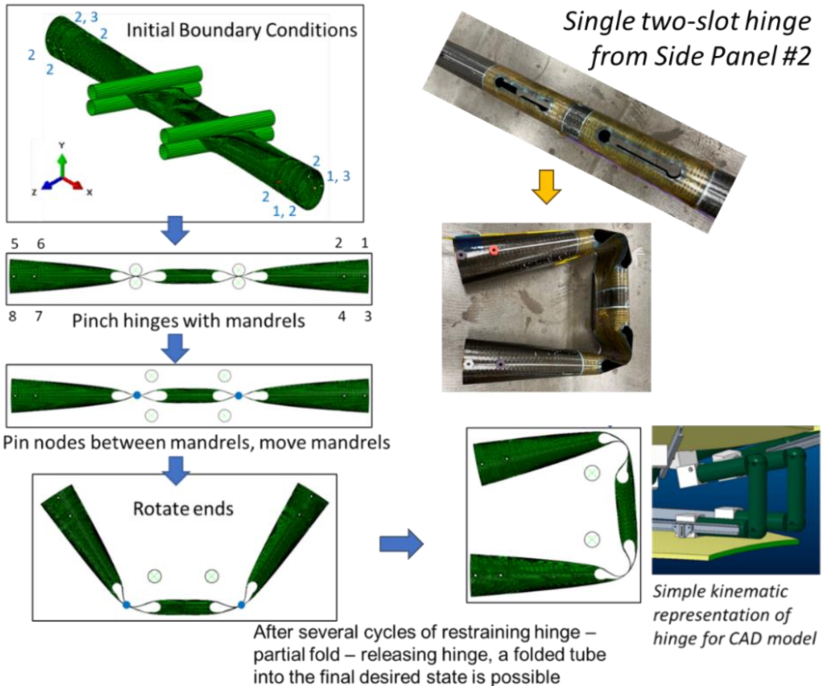

Fig. 9. Quasi-static folding steps of a two-slot hinge into the desired stowed configuration for subsequent dynamic deployment study. The top right images show the actual hinge before and after folding.

IV. Fabrication

A. Shape Memory Composite Tubular Hinges

The proposed reflector architecture required fabrication advancements in several areas to produce parts with the required thermal and dimensional stability characteristics. The tubular hinges require integrated heaters for actuation of the SMC material, as well as temperature sensors for closed-loop control, and strain sensors to confirm deployment. Pennsylvania State University (PSU) developed custom ultrathin-film heaters to NASA specifications for this project. They were produced using a new microfabrication process [13], and have a total thickness of 26 µm: 12 µm polyimide substrate, 9 µm copper active layer, and 5 µm polyimide encapsulation. The heaters have the required dogbone slots and multiple units are joined by microfabricated leads to yield an integrated part that can be embedded directly into the laminate stack, as shown in Fig. 10 (b), or placed on the outside of the tubes, as shown in Fig. 9. The lead ends protrude outside of the SMC hinge so that electrical connections with the rest of the panel hardware can be made.

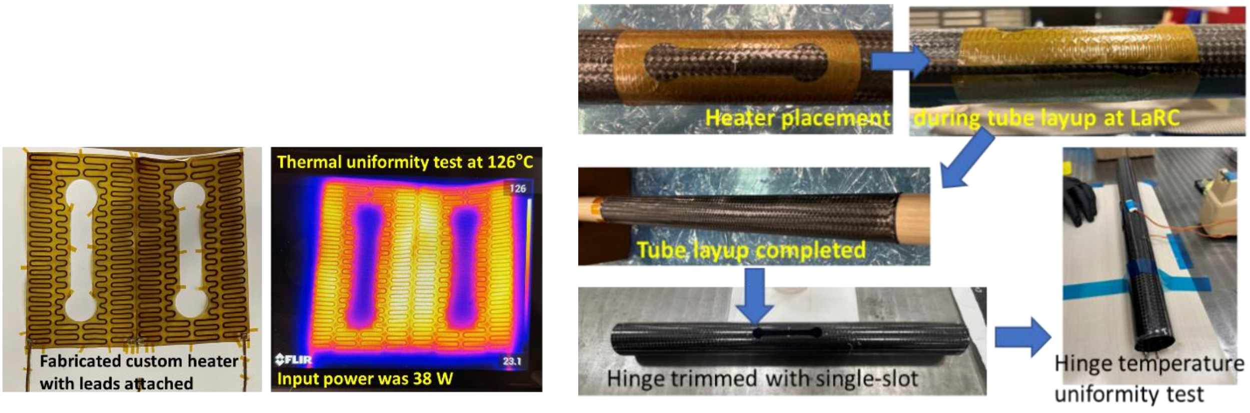

(a) (b)

Fig. 10. (a) Custom ultrathin-film heater produced by PSU; and (b) fabrication process steps of the SMC hinge with the heaters embedded. Temperature uniformity tests were carried out before and after integration of the heaters in the hinge.

Temperature uniformity tests at the minimal operational temperature of 125 ºC of the SMC material were carried out prior to assembly. Under room temperature conditions, each heater unit requires 38 W of power to reach the minimum operational temperature. However, since the heaters do not span the entire hinge region to be folded, a larger input power of 65 W was used to reach a max temperature of about 160-170 ºC at the heater locations to guarantee a minimum SMC actuation temperature of 125 ºC everywhere else. For the single and two-slot hinge this translates to about 65 W and 130 W of power for about 45 s to actuate the hinge. Some of the steps of the fabrication process of the SMC hinge are shown in Fig. 10 (b), including the final temperature uniformity tests carried out with surface-bonded thermocouples and a laser thermometer.

B. Hexagonal Reflector Panels

The hexagonal rigid panels that form the reflective surface of the parabolic reflector were designed using a sandwich construction approach to yield a high specific stiffness construction. Two sets of panels were fabricated. A first set that served as the rigid panels of the proof-of-concept breadboard test article for the new reflector architecture was produced from 12.7-mm-thick core, which were precision machined out of carbon foam (CFOAM 30®). This foam material has a density of 480 kg/m^3 and a coefficient of thermal expansion (CTE) of 5 μm/(m·K) at temperatures above 200 ºC. This is of the same order of magnitude of the CFRP face sheets that are bonded to it, resulting in minimal thermal expansion mismatch. These thin panels were fabricated such that the target paraboloid reflective surface was on the convex side of the panels instead of the concave surfaces. The reason being that they were also to be used as future molds for lighter versions of the hexagonal panels that would be fabricated onto the convex side such that those had the desired curvatures on their concave side.

The machined carbon foam cores were sealed with ES-215 epoxy resin mixed with IHG hardener that is typically used in high temperature composite tooling. The 0.18-mm thick CFRP face sheets were co-cured directly onto the cores and bonded in a single step using a 0.08-mm-thick EA9696 epoxy film adhesive. The face sheet is a four-ply balanced and symmetric plain weave laminate with the thinnest design possible to ensure that dimpling on the core would not be a problem for high accuracy applications. Each hexagonal panel has a mass of ~6.3 kg with 85% of its mass being the core. A good rule of thumb to maintain adequate hexagonal sandwich panel stiffness is to make the core thickness proportional to the panel width (corner to corner) [4]. The machined core thickness of 12.7 mm could be reduced further but was not chosen for the exploratory two-panel assembly breadboard demonstrator to maintain panel precision during manufacturing and during thermal loading. The central and side panels were manufactured with a root mean square error (RMSE) from the nominal of 0.30 mm and 0.78 mm, with the corner areas showing largest deviations of 1.15 mm and 1.45 mm, respectively. A Creaform Go! SCAN 3D handheld laser scanner with a volumetric accuracy of 0.05 mm + 0.15 mm/m and 0.10 mm resolution was used to scan the working surfaces of the panels. Most of the manufacturing error was attributed to the machining process of the cores, where, given their thinnest, they had to be fixed to tooling while operated on, which gave rise to internal stresses that relieved after the final acceptance metrology occurred.

The second set of hexagonal panels manufactured use 7.9-mm-thick carbon honeycomb core and other flight-grade materials purchased from Patz Materials and Technologies. The ultralight cores have a 32 kg/m^3 density and are constructed from high modulus YSH-50A carbon fiber fabric and PMT-F7C epoxy resin using a ½” CRV flexible cell geometry. This unique cell geometry allows the material to conform to complex shapes with far less splicing, and the interlocking design makes seamless installations simply by bonding individual panels together node-to-node. The total mass of each ∼1 m^2 area sandwich panel is about 1 kg, resulting in a seven-panel assembly at the 3-m-diameter scale of about 20 kg, including backside-attached hardware (SMC hinges, gap closing mechanisms, and launch locks). These lighter panels were designed such that the first natural frequency of the entire deployed reflector in zero gravity conditions and anchored from one end of the reflector is above 1 Hz. One of the panels with carbon honeycomb cores is shown in Fig. 11 along with some of the fabrication steps. A full set of seven 1 m^2 panels have been manufactured to assemble a complete 3-m diameter brassboard reflector for final proof testing. The panel manufacturing errors are shown as deviation contour plots from the nominal paraboloid surface in Fig 12. The positive (in red) and negative (in blue) are where the fabricated panel is above and below the nominal reference panel. A RMSE from the nominal of 0.29 mm and 0.27 mm for the central and side panel was measured using the same Creaform handheld scanner. Both panels have a characteristic saddle shape with different sign curvatures along two opposing corner areas, showing local deviations up to 1 mm, in part due to the original mold error.

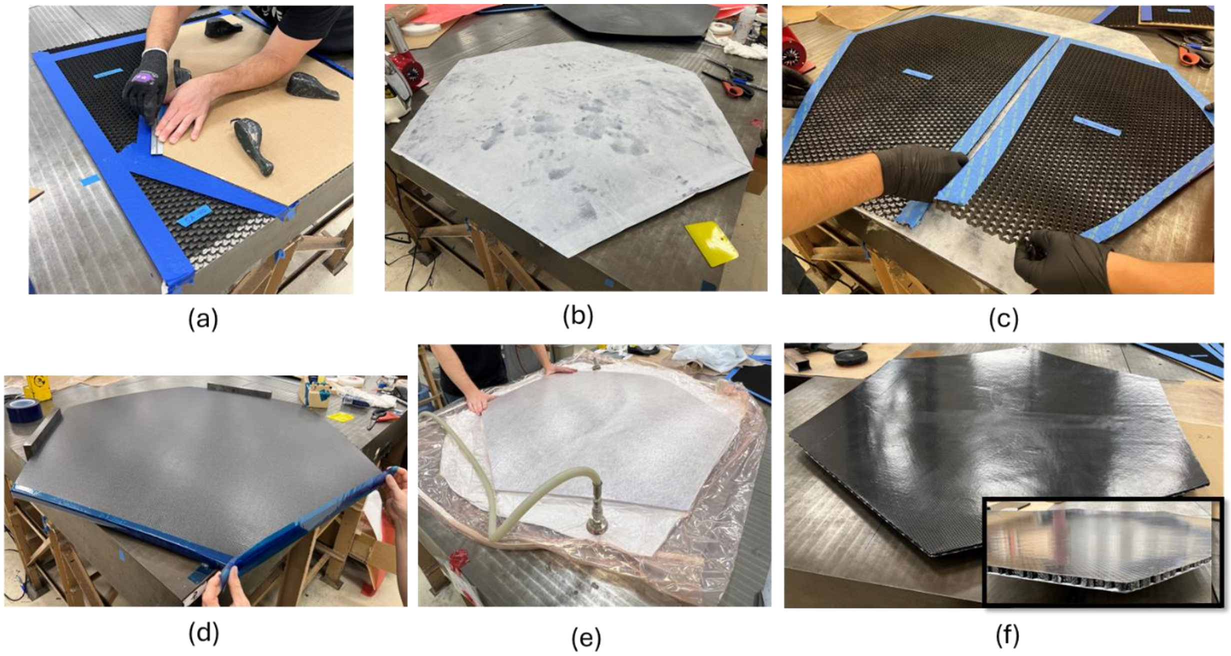
(a) (b) (c)
(d) (e) (f)

Fig. 11. Some fabrication steps of the lightweight construction reflector panels: (a) Slicing of honeycomb carbon core segments to form the hexagonal panel layout; (b) Placing the cured bottom CFRP face sheet against the reflector mold and a layer of PMT-F7-AF film adhesive on top; (c) Placing the segmented core onto the film adhesive; (d) Draping another layer of adhesive and the cured top CFRP face sheet on top using aligment plates and covering the panel free edges with tape to prevent the stack shearing; (c) Vacuum bagging the entire stack assembly for autoclave processing; (f) Cleaning and sanding edges of the final sandwich panel.

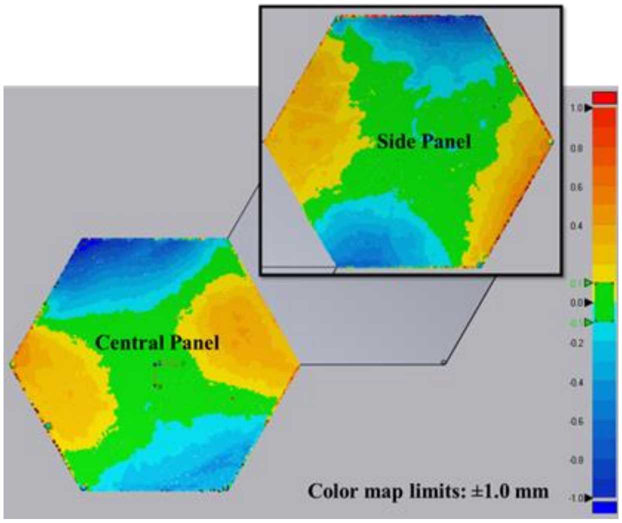

Fig. 12. Carbon honeycomb core sandwich panel manufacturing error plot for the central and side reflectors.

V. Initial Test Campaign Results

The two heavier sandwich panels were used for a proof-of-concept testing campaign whose goal was to increase the new reflector architecture and flexible composite substrate to a technology readiness level (TRL) of 3. This involved assessing the critical functions and characteristics of the new components analytically and experimentally. Priority was given to producing subscale breadboard articles with representative features and functions to validate the fabrication process and the conceptual design and obtain needed information for future analysis and tests to TRL 4. The two main test objectives were to: 1) Determine the feasibility of elastically folding and unfolding the new composite substrate design (SMC hinges) that will have a permanent connection between rigid segmented panels of a large RF reflector as provided by Maxar Technologies; and 2) Perform tests and analysis that demonstrate the breadboard unit being folded and unfolded.

A. Test Setup

A two-panel reflector assembly representative of the central panel and Side Panel #2 in the vertical stack was produced. First, the pair of SMC hinges deploy until straight, followed by the side panel moving into final position via the secondary mating mechanism. Initially, environmental deployment tests were planned inside LaRC’s large 2.4 m diameter, 5 m long thermal-vacuum (TVAC) chamber to remove convection heat transfer for improved SMC hinge actuation, and to provide additional thermal input if needed. However, the component hinge testing determined that the custom heaters were capable of effective SMC hinge actuation in ambient conditions at increased power levels so these TVAC tests were removed. Due to budget restrictions, the gravity off-loading system was to be shared between this test article and another one for an alternative reflector concept under evaluation [14], so a vertical deployment configuration was preferred, such that the deployment path occurs along a straight line for ease of panel off-loading.

The final test configuration had the central hexagonal panel fixed with the convex side up on a pedestal and the side hexagonal panel stowed on top of it with the concave reflective side up. The two panels were connected by a pair of two-slot SMC hinges corresponding to the second side panel in the stack and a secondary panel mating and latching mechanism. The initially planned test configuration inside the TVAC chamber is shown in Fig. 13 (right), and the final test configuration in ambient in Fig. 13 (left). The mass of the side panel assembly including the backbone hardware attachment was 9.3 kg. The side panel was supported by an aluminum extruded U-frame that translated along the linear deployment path and allowed free rotation of the side panel on bearings about the axis connecting two of its opposing corners as needed for the panel to swing ~180° and end with the concave side down. Significant effort was required to balance the panel test article about the axis of rotation for all orientations. Ballast masses were added to the moving side panel to balance it. The aluminum U-frame was suspended from a pulley system that travelled lengthwise using a trolley riding on an overhead conveyor track. The weight of the panel assembly was offloaded by a counterbalance hanging mass on the other end of the two-pulley system.

During pre-test preparations, it was found that friction in the overhead trolley system was unacceptably large, and given the total weight of the moving test article that included the heavy aluminum U-frame, the hinges were not going to have enough self-deployment force to move the assembly. Therefore, some manual operator input to the counterweight was necessary to break static friction at the start of the test, and minimally throughout the test to help translate the mass along the overhead track. During the ~180° rotation of the moving side panel, it was identified that the counterweight mass had to be reduced by 4 kg to result in a near-zero net uplift force at the 90° rotation stage of the panel, i.e. for the first 90° of side panel rotation when the panel assembly moves upwards, the mass was 4 kg heavier than for the second 90° rotation when the panel assembly moves downwards. The change in vertical motion of the offloading line meant that the pulleys needed to rotate in opposite directions during the test, and thus the 4 kg reduction in mass was needed to cross the pulley system deadband around 90° and generate the complete moment-vs-rotation plot. The manual operations during the deployment of the moving panel by the two test operators were rehearsed several times to minimize errors and test-to-test variations.

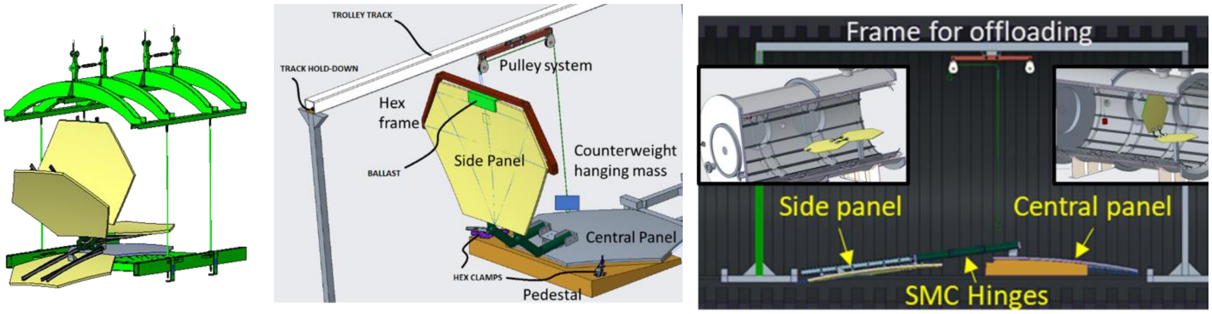

Fig. 13. Vertical deployment test configuration of the two-panel assembly inside the thermal chamber for final validation of the system. From left to right, the images show various snapshots during the deployment phase showing the side panel in the initial, upwards, and final state of deployment of the tubular hinges prior to actuation of the secondary mechanism to close the panel-to-panel gap.

Shape measurement scans of the non-reflective surface of the panels pre-and-post deployment were used to assess feasibility to support S-band and above RF (≥ 2 GHz frequency) at the 3-m reflector size scale by determining if a surface RMSE of < 3 mm was attainable. The same portable scanner used to measure the individual panels was used for the post deployment test scans. In addition, the SMC hinges and their end fittings were random speckle painted such that two pairs of photogrammetry cameras tracked their motion via digital image correlation (DIC) using the Correlated Solutions’ VIC 3D software. Three direct current (DC) power supplies were used. Two units, each with two channels with the power output set at 28 V and 2.3 A for each of the SMC hinges, and one unit with an output set at 12 V and 0.75 A for actuation of the TiNi FD04-4605 Frangibolt used as a launch lock simulator. The test setup with the panels stowed is shown in Fig. 14 (left). The deployment sequence of the pair of hinges that rotated the moving panel ~180 deg is depicted in Fig. 15, where the final configuration with the hinges unfolded straight can be seen in more detail in Fig. 14 (center).

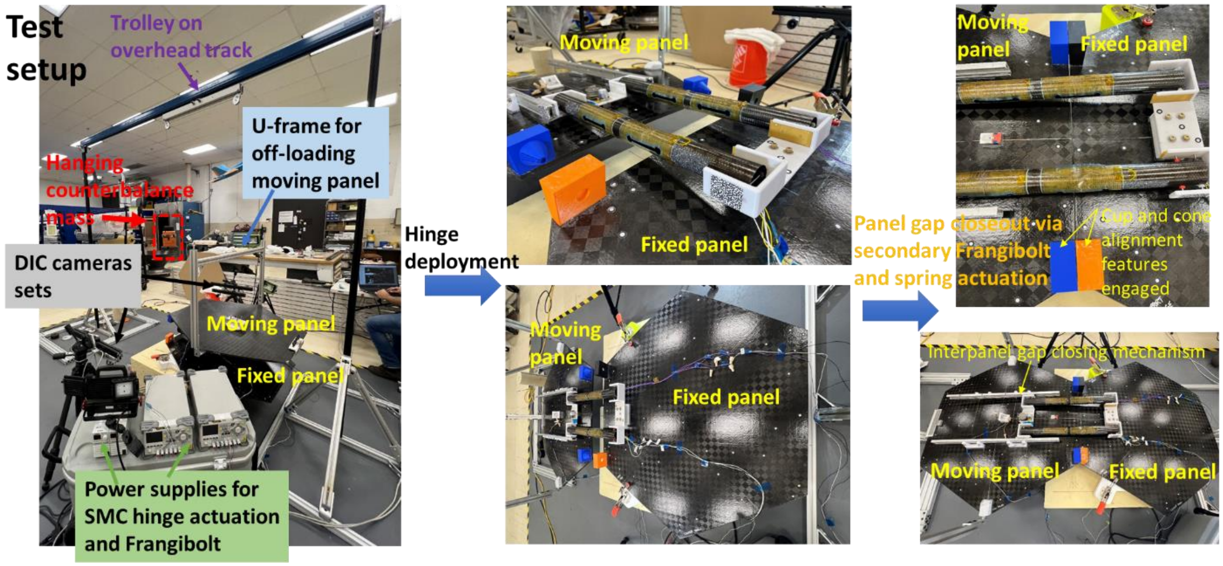

Fig. 14. Test setup (left) and stages of deployment of the two-panel assembly: hinge deployment (center) and panel gap closure and latching (right).

B. Panel Deployment Test

To start the panel deployment process, the SMC hinge pairs were brought up to their activation temperature above 125°C using the power supplies, as shown in Fig 15 (a). Point at which the operator slightly tapped on the counterweight to enable uplift motion of the side panel. The panel then began to rotate through the self-deployment of the SMC hinges while translation of the aluminum U-frame along the overhead track was enabled by the trolley with the pulley system; Fig 15 (b). When the side panel reached a vertical orientation, 4 kg of the counterweight were removed by one operator to start enabling downward motion of the panel; Fig. 15 (c). The panel continued its swivel and when it was at a ~130° rotation, the outer slots of the hinges (further away from the central panel) snap-through to the extended state while the inner slots were still partially folded; Fig 15 (d). The start of the snap-through event of the inner slots of the hinge pair began at a ~160° panel rotation angle; Fig. 15 (e). The panel at the end of deployment (~180° rotation) with the hinges locked straight is shown in Fig. 15 (f). At that moment, the heater power was turned off and the hinges cool down and regained their rigid load-bearing state. Two deployment tests were successfully carried out to assess the feasibility of the concept.

The three-dimensional (3D) displacements of the moving panel and two hinges were tracked by the two VIC 3D photogrammetry DIC systems, each observing one of the hinges. The longitudinal (x-axis) and vertical (y-axis) displacements of the end of the right (R) and left (L) hinges fixed to the moving panel are shown in Fig. 16. The z-axis data is omitted as lateral displacement were negligible due to the mostly planar motion. The Basler acA3088-16gm GigE photogrammetry cameras used were recording at their maximum 16 frame per second (fps) rate. The relatively fast speed of two events were not tracked due to loss of correlation of the native images that appeared blurred. The first event corresponds to an approximate 2.5 s time span when the panel rotation angle changed from 25° to 35°. The two-slot hinges were in their low moment region, shown as a plateau in the moment-vs-rotation graph in Fig. 7, and the panel motion is mainly counterweight driven, which is subjected to manual operator input and inertial effects. The second event where data was lost is the end of deployment when the hinge fully snapped back to the final straight configuration. This was an energetic dynamic event and would have required cameras with a larger fps capability. The region where the panel reached the vertical upright orientation is shown by the peak in y-displacement.

This event was followed by a few seconds were the panel was held static while 4 kg of counterweight were removed to enable downwards motion. The last dynamic event when the outer slots of the hinges recovered their straight configuration is also visible by the change in slope of the y-displacement data.

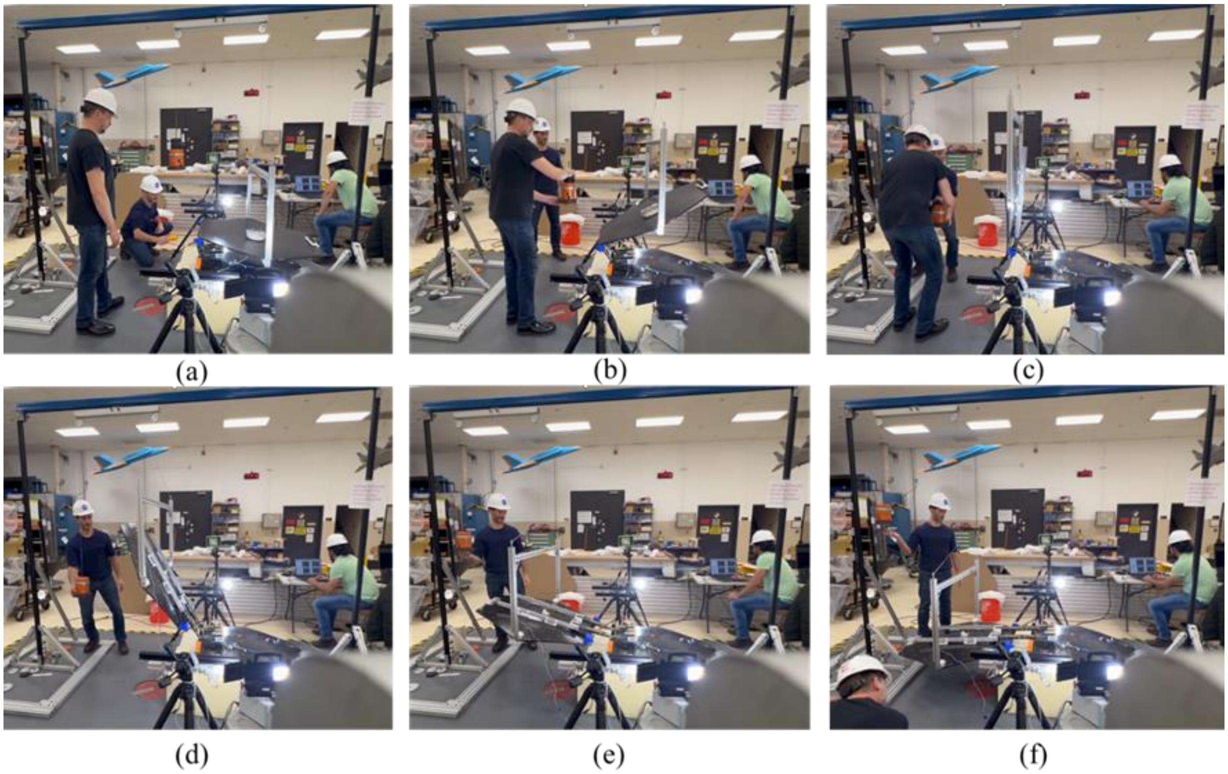
(a) (b) (c) (d) (e) (f)

Fig. 15. Deployment sequence of the two-panel assembly: (a) monitoring heater temperature prior to SMC hinge actuation; (b) panel at 30° rotation; (c) panel at 90° rotation (vertical), when the 4 kg of counterbalance mass was removed; (d) panel at 130° angle just after the snap-through event of the outer slots of the hinges; (e) Panel at 160° rotation just before the inner slots of the hinges snap through; (f) Panel at the end of deployment (180° rotation) with the hinges locked straight.

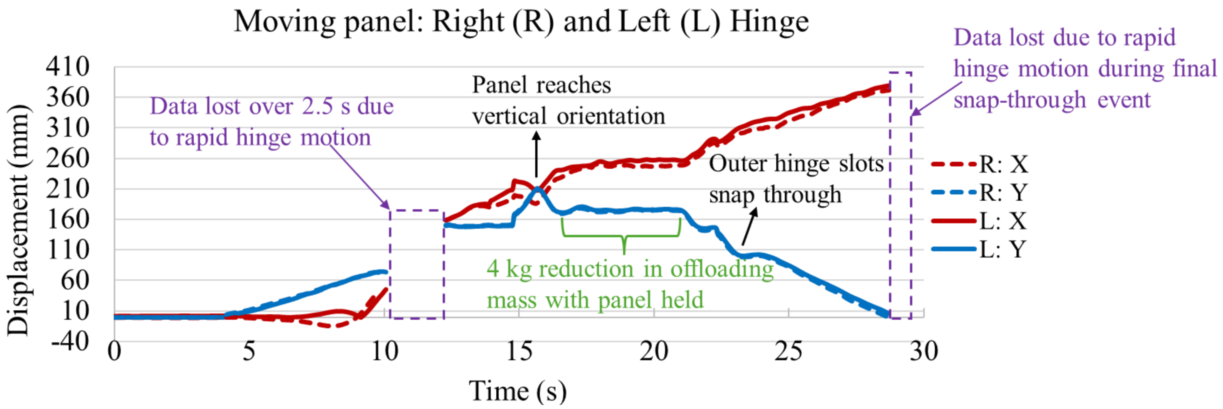

Fig. 16. Displacements of the end of the right (R) and left (L) hinge fixed to the moving panel during deployment as tracked by the DIC system. X is the longitudinal axis between panels and Y is the vertical axis. The Z axis data is not shown as values are near zero (2D deployment).

C. Panel Latching Test

The second phase of deployment consisted of closing the gap between the central and side panels left by the hinges rotation process. The side panel was spring loaded using a lanyard reel with a clock spring that provided a near constant 13-N force. This force was used to close the gap once the launch lock was actuated. The hold down release mechanism used was a TiNi Frangibolt that cut the bolt fixing the hinge end-fitting trolley to the side panel. Upon release, the trolley was able to slide along the two fixed guide rails closing the panel gap, as identified in Fig. 2. Two large cup and cone alignment features with latching features fixed to the backside of the panels were used to mate the panels and secure them in the final desired assembled state.

The same photogrammetry DIC setup was used to track the mating process of the panels. The displacements of an end section of the rail of the moving side panel during the closing event tracked by the right (R) and left (L) DIC systems are shown in Fig. 17. X is the longitudinal axis between the panels, Y the vertical axis, and Z the lateral axis about which the side panel initially rotated about. The purple highlighted region indicates when the cup and cone engaged to align the two panels. Snapshoots taken at the start, middle and end of the panel motion from the left stereo-camera system are also shown to reveal the region of interest on the rail, and the cup and cone alignment elements. To mate the panels, a total of ~150 mm x-translation of Side Panel #2 was needed. This distance will vary from panel to panel in the reflector vertical stack. In general, there was small difference between the left and right DIC displacement data.

A first unsuccessful attempt of the panel mating event revealed that in order for the interpanel gap to close, the center of gravity (CG) of the side panel test article plus the U-frame needed to be artificially moved forward approximately half of the x-distance to create an offset between the edge of the side panel and the z-rotation axis of the panel. Otherwise, as the side panel and the aluminum U-frame moved along the rails, the CG translated along the x-axis causing a z-axis gravity-induced moment on the side panel that raised the cones and missed the mating cup features of the fixed panel. The y-axis vertical displacement data in Fig. 17 reveals the mating end of the side panel first vertically moving down and then up. The inflection point in that curve occurred at approximately one-half of the x-distance to close, and is the configuration where the CG of the test article was balanced about the aluminum U-frame axis during panel translation. This complex motion and balance tuning process exemplifies how important it is to determine a priori the moments induced by gravity on the offloading support hardware that can hinder the correct performance of the test article.

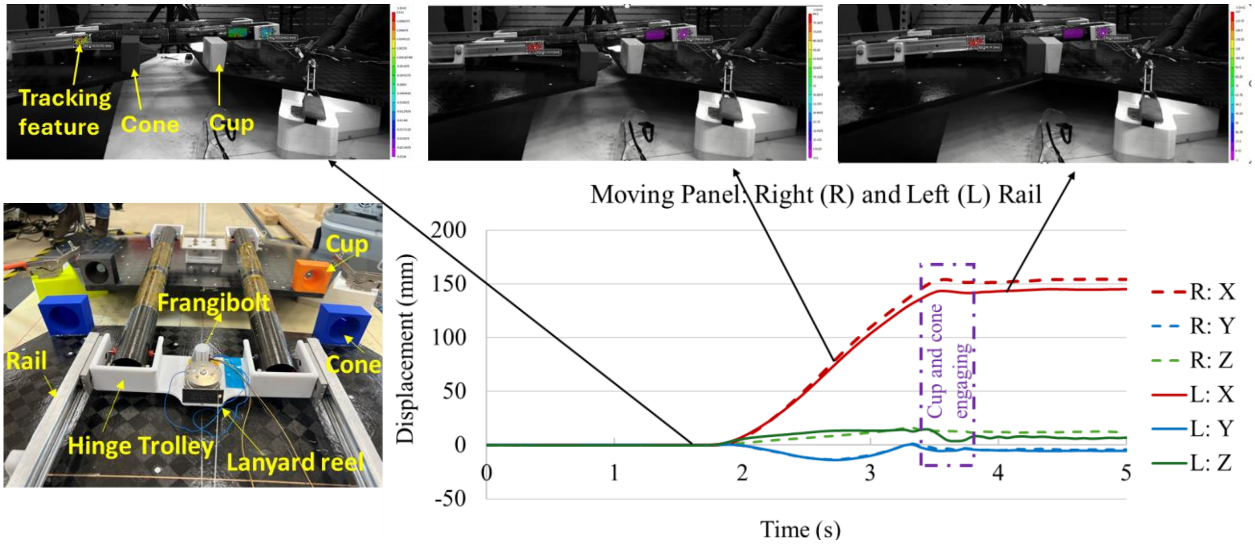

Fig. 17. Displacements of the end of the rail of the moving panel during the panel closing event tracked by the Left (L) DIC system. X is the longitudinal axis between panels, Y the vertical axis, and Z the lateral axis. The purple highlighted region indicates when the cup and cone engaged to align the two panels. The top images show snapshoots from the start, middle and end of the panel translation, indicating the region of interest used for tracking and the mating elements. The bottom left image shows the various components of the panel closing mechanism before actuation.

D. Metrology Results and Conclusions

After the panel deployment and latching tests, 3D surface scans of the mated panel assembly were taken. Given the test article orientation, the backside of the reflector panels was scanned and used for correlation with the pre-test scans taken before the stow and deployment functional tests. The post-processed metrology data showing the deviation color plots of the functional tests are shown in Fig. 18. The left and right image differ by the limits of the color plot. The left image with ±14 mm limits, reveals a relatively linear gradient up to +13 mm deflection at the side panel end due to insufficient ballast mass artificially pulling this end upwards. This shows the great negative effect that the gravity offloading system configuration designed for an optimal deployment process (enable panel latching) can have on post-deployment measurements. In this case, it would have been advised to rebalance the panel after deployment such that no artificial moment about the aluminum frame was present during final shape measurements. The right image color map limits reveals the deflection around the joint line between the panels. The highlighted region consisting of a 50-mm-wide slice of the side panel was used for local RMSE measurement, which was found to be 0.46 mm. Similar metrology data for the comparison of the post-deployment surface scan to the nominal two-panel assembly shape, also known as the total deviation, showed a local RMSE on this panel joint line of 2.61 mm. Given the average side panel manufacturing error of 0.78 mm with local maximums of up to 1.45 mm along the mating edge of the side panel, and the functional test error shown in Fig. 18, the total error finding highlights that a large part of the deviation was due to the initial assembly of the panels, revealing the need for better assembly tooling to define the initial state of the side panel moving forward. The same gravity off-loading system was used during the initial panel assembly and scan that once more tended to pull up the free end of the side panel. Note that no fixturing was used to define the position of the side panel end during this exploratory test campaign.

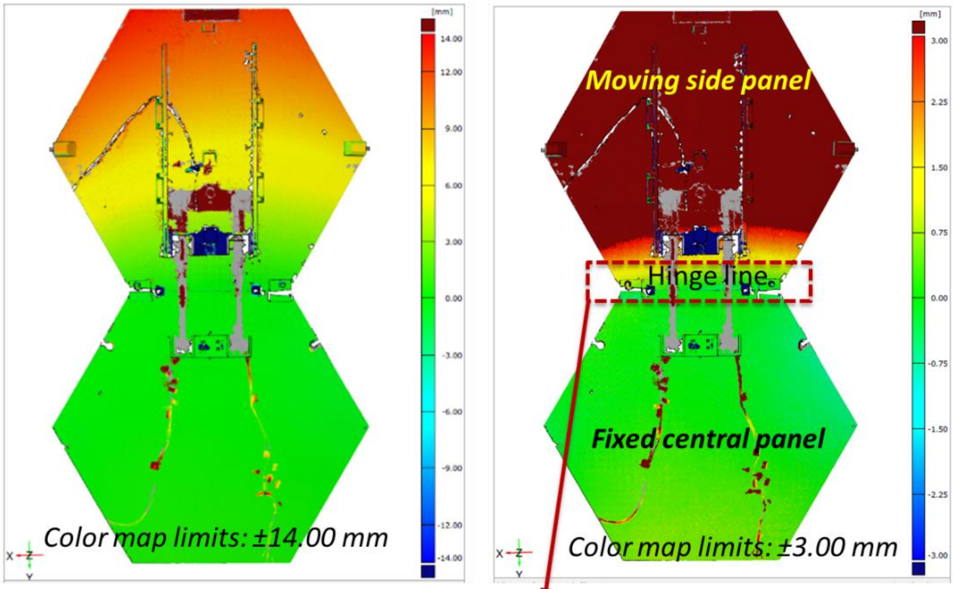

Linear gradient up to +13 mm deflection at side panel end due to the insufficient ballast mass artificially pulling upwards this end

Region of interest (panel joint) with local RMSE: 0.46 mm

Fig. 18. Two-panel assembly stow and deployment functional test error. The color plots show the deviation of the post-test surface scan with respect to the pre-stow and deployment scan. The red and blue indicate where the post-test panel assembly is above (out of the page) or below from the pre-test assembly. The left and right graphs have ±14 mm and ±3 mm deviation limits. The region of interest (panel joint) is highlighted in the right image showing a local RMSE of 0.46 mm.

The primary lessons learnt from the initial test campaign and the future design and test recommendations were:

1. The heater temperature should be kept below 170°C in the SMC hinges to avoid heater debonding. The use of a higher temperature adhesive would provide more margin between adhesive softening temperature and SMC actuation temperature.
2. The chosen vertical panel deployment configuration overcomplicated the test due to the rotating panel having to change orientation with respect to the gravity field. It is preferred to have dedicated ground support equipment (GSE) for the panel-assembly test article and use a horizontal panel deployment configuration such that gravity acts parallel to the rotation axis of the hinges/panels, not inducing moments about it.
3. Friction in the GSE offloading system (tracks and pulleys) needs to be reduced significantly given the low actuation forces of the SMC hinges. Once panel mass is reduced significantly, the use of helium balloon off-loading lines would be a good approach for the horizontal deployment configuration because the balloons would minimally restrain the test article.
4. Precision panel mating components with locking features are critical to guarantee proper panel alignment is maintained, even when there is panel preload. More flight like mating components should be used in the next iteration and their optimal placement studied.

5. Cameras with higher frames per second (fps) are needed to capture the dynamic events of the hinges, particularly final snap-through. A minimum of 50 fps is required to track these fast events.
6. The panel assembly pre-test configuration needs to be improved by the use of an assembly fixture and not just the use of the panel mating alignment features at the joint line in order to reduce initial deviation with respect to the nominal assembly.
7. The panel assembly post-test measurements should not be influenced by gravity where possible. The GSE off-loading system should not be over or under correcting the gravity induced moments in the final locked stage of the panels.

The goal of the initial subscale breadboard prototype test campaign was to assess the effectiveness of the novel key features of the reflector that would be used in future designs up to the 10-m scale to enable efficient stowage with minimal constraints, controlled deployment, and maintain the necessary on-orbit shape accuracy of less than 3 mm RMSE. The results were considered to be promising and it was believed that with attainable improvements in panel fabrication and assembly, and gravity off-loading system, the next iteration of the reflector under development could demonstrate the less than 1 mm RMSE surface accuracy needed to support X-band and higher radio frequency transmissions (≥ 8 GHz) at the 3-m and above scale.

VI. Final Reflector Design and Test Campaign Results

A. Final Reflector Design

A subsequent effort started in 2024 at LaRC with the goal to mature the reflector technology to TRL 4/5. A complete 3-m diameter hexagonal reflector was manufactured using flight-grade materials. Modal analysis of the deployed configuration of the reflector using a PATRAN/NASTRAN finite element model revealed that the honeycomb core thickness would have significant effect on the first several natural frequencies of the reflector. Sandwich hexagonal panels with a 32 kg/m^3 carbon honeycomb flex core and 0.18-mm-thick high modulus carbon fiber woven laminate HS40/PMT-F7 face sheets arranged in a balanced and symmetric stack were modeled.

A panel trade study with 6.35 mm, 7.93 mm and 9.52 mm core thicknesses was performed. The total mass of the seven-panel reflector is dominated by other elements and remained within a 24.5-25.3 kg range for all cases. A MAT2/PSHELL material card was used in NASTRAN to define the 3D orthotropic properties of the honeycomb core. Fixed boundary conditions in all six degrees of freedom were applied to either the center of the central panel or at a far edge of the -X side panel to simulate the connection to the reflector or the spacecraft offset boom, respectively. Unloaded cases and cases with Earth's gravity (1g) acceleration applied in all 3 axis (X, Y, Z) and two directions (+, -) were run. Note that center Z-axis and edge X axis cases (Fig. 19) are most likely to be used in ground testing.

The first three modes for each boundary condition under 1-g loading are presented in Fig. 19. Analysis results showed that the edge supported cases had an order of magnitude lower first frequencies than the center supported cases. The 7.93-mm-thick core was selected for manufacturing to meet the goal of having the 1st natural frequency above 0.5 Hz and 1 Hz for 1-g and 0-g loading and far edge support. The center cases modes were all above 5 Hz. The natural frequency values were affected by the panel core thickness but the first few modes shapes remained the same for all cases.

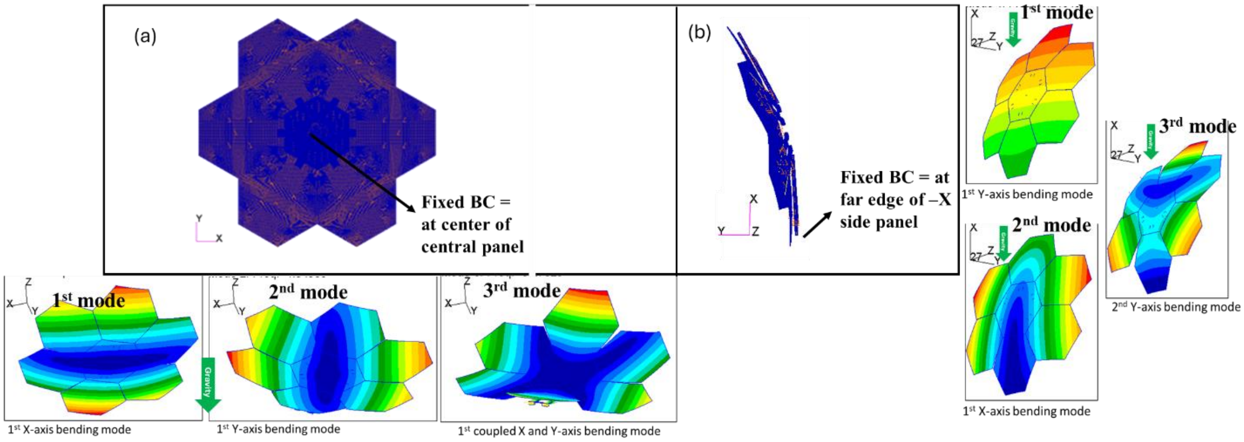

Fig. 19. Modal analysis results of the entire deployed reflector for two fixed boundary conditions and 1g acceleration directions: (a) center of the central panel with 1g on -Z axis; (b) far edge of the -X side panel with 1g load on -X axis. Contour color plots of the first three mode shapes are also shown.

B. Panel Assembly and Alignment

An improved assembly process for the two-panel configuration was sought to decrease the previously observed pre-test assembly error. First, each fabricated reflector panel was scanned individually and compared against the nominal design, as shown in Fig. 12. Spherical targets with 14 mm diameter were added to the four free corners of each panel in addition to the midspan location of the far edge of the panel. These five targets were used for best fit or datum alignment between a reference and a measured part in the Geomagic metrology software from Oqton. A best fit alignment uses a least square algorithm to align tow point sets by transforming one of the sets so that the sum of the squared distance between matching points in the two sets is minimal. This causes a set of measured points or actual feature centroids (sphere centroids in our case) to match as closely as possible to its nominal location or theoretical counterpart. The nominal assembly as provided by the computer aided design (CAD) model of the two-panel test article that included the modelled spheres was used as the reference model. A best fit alignment of the two imperfect panels against the reference assembly model provided the nominal assembly against which all the subsequent physical scans of the assembly during the panel alignment process would be compared.

Dedicated fixturing was designed to perform both a first rough panel alignment and make fine alignment adjustments. The hardware used is shown in Fig. 20 (a). An optical bench with 25.4 mm hole spacings was used as a adequately flat working surface. Each panel was supported by three pedestals: two near the panel corners of the joint line and one towards the back end of the panel at its symmetry line. These pedestals were spring-loaded such that a constant downwards force kept the panels fixed against them. The central panel rested on pads and was considered fixed during the panel alignment process. The side panel rested on precision ball-head screws with 170 turns per inch so that one full turn resulted in about a 0.15 mm height adjustment. For the first rough alignment, side plates that were 3D plastic printed from the nominal assembly model were used for lateral adjustment. Another 3D printed element placed spanning across the top of the panels along the longitudinal symmetry line was used to define an initial pitch angle of the side panel.

The reflective concave surfaces of the central and side panels were measured with the previously used Creaform handheld scanner. The surface deviation contour plots for various alignment steps of the side panel are shown in Fig. 20 (b). The reference surface is the best fit as-manufactured panel assembly. At least three of the spheres on the fixed central panel were used to produce a best-fit alignment of the scanned and reference central panel. It can be seen that the side panel progressively achieves a better alignment against the nominal surface. However, it was not possible to further improve the alignment as the deviation contours had the maximum error away from the screws, as shown in the final plot. The left corner of the side panel appeared low and the right corner high with min/max values of about 0.6 mm. The RMSE of the final panel alignment assembly is 0.716 mm.

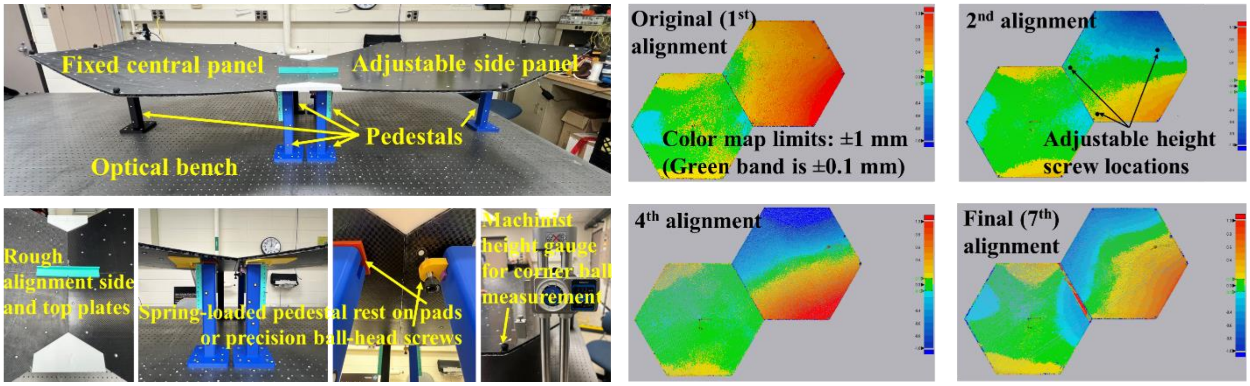

(a) (b)

Fig. 20 Assembly of the two-panel test article: (a) Hardware used to provide rough and precise alignment of the panels, which include side and top plates, precision ball-head screws, spring-loaded pedestals and a machinist height gauge; (b) Surface comparison deviation plots between the reference panel alignment and the measured scan for various alignments. After the original 1st rough alignment, only the three height adjustable precision screws under the side panel shown in the first image were fine tuned to decrease the error.

Once the two panels were aligned, cup and cone assembly features seen in Fig. 21 were bonded in place to the central and side panels, respectively. The cup and cone elements were improved designs of the elements used in the initial breadboard test campaign and acted as a kinematic mount by implementing a set of three V-grooves and ball couplings that constrained all degrees of freedom (DoFs = 0) when engaged. The cup element had three conical cups that each housed a precision V-groove mount at their end. The cone element had three matching cones that each housed at their end a precision ball that was glued in place once the cup/cones were initially mated pre-assembly. The kinematic mount was designed using the Maxwell criterion to optimize for repeatability and stability, which involves arranging the three balls in space as the vertices of a triangle and then orienting the centerlines of the V-groove mounts such that they bisect the angles of this triangle and intersect at a single unique point. This resulted in the cup and cone elements always coming together to a defined single position and orientation. The isosceles triangle was chosen with the largest height allowed by the stowed configuration of the panel to increase stability. Three magnet pairs were also included in the cup and cone parts to provide a higher mating force than the lanyard reel spring alone. The pairs of magnet faces did not come in contact when the panels mated so that it was the kinematic mount dictating the end of travel. The location and magnitude of these magnets was chosen such that the magnetic force moments created about the center of the triangle were cancelled. These components can be seen in Fig. 21.

The process of adding these cup and cone elements to the two aligned panels consisted of fixing the side panel on the optical bench and removing the central panel so that a cup element could be bonded along the mating edge of the central panel. Then, the central panel was brought back to the optical bench setup, and the cone hardware was mated to the cup hardware using the precision mounts, while under compression load applied by clamps. Lastly, the bottom surface of the cone element was bonded with paste adhesive to the side panel, while under load. Two final surface scans of the assembled test article were taken. One after bonding once the clamps were removed, and another after the panels were detached and then manually mated again. The first of these scans is considered the pre-test assembled shape of the panels.

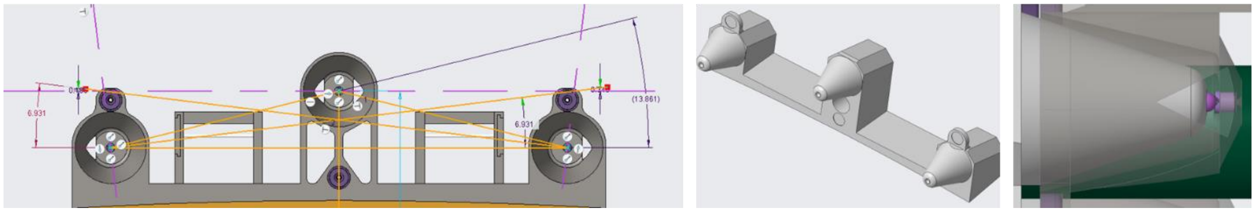

(a) (b) (c)

Fig. 21 Kinematic mount for panel mating: (a) Front view of the cup element showing the location and orientation of the precision V-groove mounts. The central cup has the V-groove oriented vertically, and the two side cups angled at 7° from the horizontal plane, such that the orientation of the three V-groove couplings define a unique point in space, which is at the center of the yellow triangle shown; (b) cone elements with the precision tip balls; (c) mated assembly showing the ball and V-groove elements engaged.

C. Test Setup

The deployment test was conducted in the horizontal panel deployment configuration, with the rotation axis of the hinges parallel to gravity. The central hexagonal panel was bolted on its concave side to a rigid "main truss" at four anchor points. The 1.5-m long, 0.5-m bay size truss made of metal tubes and nodes was cantilevered in a horizontal configuration from a metal backstop wall with T-slots built into the test facility. These arrangements are shown in Fig. 22 (a) and (b).

The top view DIC camera pair was fixed to an upper truss directly above the main truss. These cameras are shown in Fig. 22 (b) and (c). The photogrammetry cameras used were Basler ace U acA1920-155um models with 2.3 MP resolution up to 164 fps rate and fitted with 35 mm and 25 mm fixed focal length lenses from Computar and Schneider for the top and bottom DIC camera systems, respectively. The two pairs of cameras were synchronized using an external signal generator with a square wave. A maximum of 50 fps were reliably achieved for all four cameras at the resolution and ~1 m field of view required to track the behavior of the two tubular hinges during the tests. Full-field strain, curvature, and displacement data of a section of the hinge was gathered using VIC 3D software from Correlated Solutions.

A Vicon videogrammetry system was employed to track the motion of the test article during the tests via 14 mm spherical retroreflective passive targets attached to the panels. A total of six Vicon Valkyrie16 cameras were used to cover the working volume, guaranteeing that during panel motion at least three cameras were viewing the spherical targets at all times. Three cameras were fixed on the backstop wall and three cameras were positioned around the approximately 180° sweep path of the side panel. These cameras are shown mounted to the backstop and on 6 m tall tripods in Fig. 22 (b). The VK16 cameras emit infrared light via a strobe ring at 850 nm wavelength. The cameras are capable of 16 MP resolution at a maximum frame rate of 240 fps. Up to 240 fps they emit the largest amount of light per frame. At 480 fps the light is halved and so on. Selecting a frame rate greater than full resolution automatically reduces image size by windowing. This keeps the pixel rate the same by transmitting a greater number of smaller images per second. The cameras are capable of capturing up to 2000 fps with a partial scan. The cameras are fitted with lens of variable focal length of 9.4 mm to 12.5 mm for 72° to 54° angle of view with an aperture range of 0-10 f-stop at the narrower view. For the panel deployment and latching tests a 100-120 fps rate was used with the narrower field of view setting of the lenses. The Vicon NEXUS software was used for tracking the individual passive targets and providing displacement data.

A gravity off-loading approach that minimized its influence on the behavior of the side panel during its motion was sought. Two latex balloons with a burst diameter of 2.44 m filled with Helium were used to offload the side panel from two locations near the two top side corners of the hexagonal panel. Kevlar® twisted thread was used to connect the balloons to the panel pickup points. The two balloons were height staggered to reduce their interaction by using offloading lines of different lengths, as shown in Fig. 22 (c). The side panel with all its hardware attached to the convex side had a mass of 3.75 kg. The sandwich panel itself weighted 1 kg and the majority of the remaining mass was located towards the mating end of the panel, which resulted in the balloon closest to the hinge needing to produce about two thirds of the total lift force and the other balloon one third of the lift. A plastic cup attached to each balloon line near the panel was used to add/remove ballast mass to balance the side panel about the normal axis before every tests to compensate for helium leakage. The balloons needed to be reinflated with helium every one to two days.

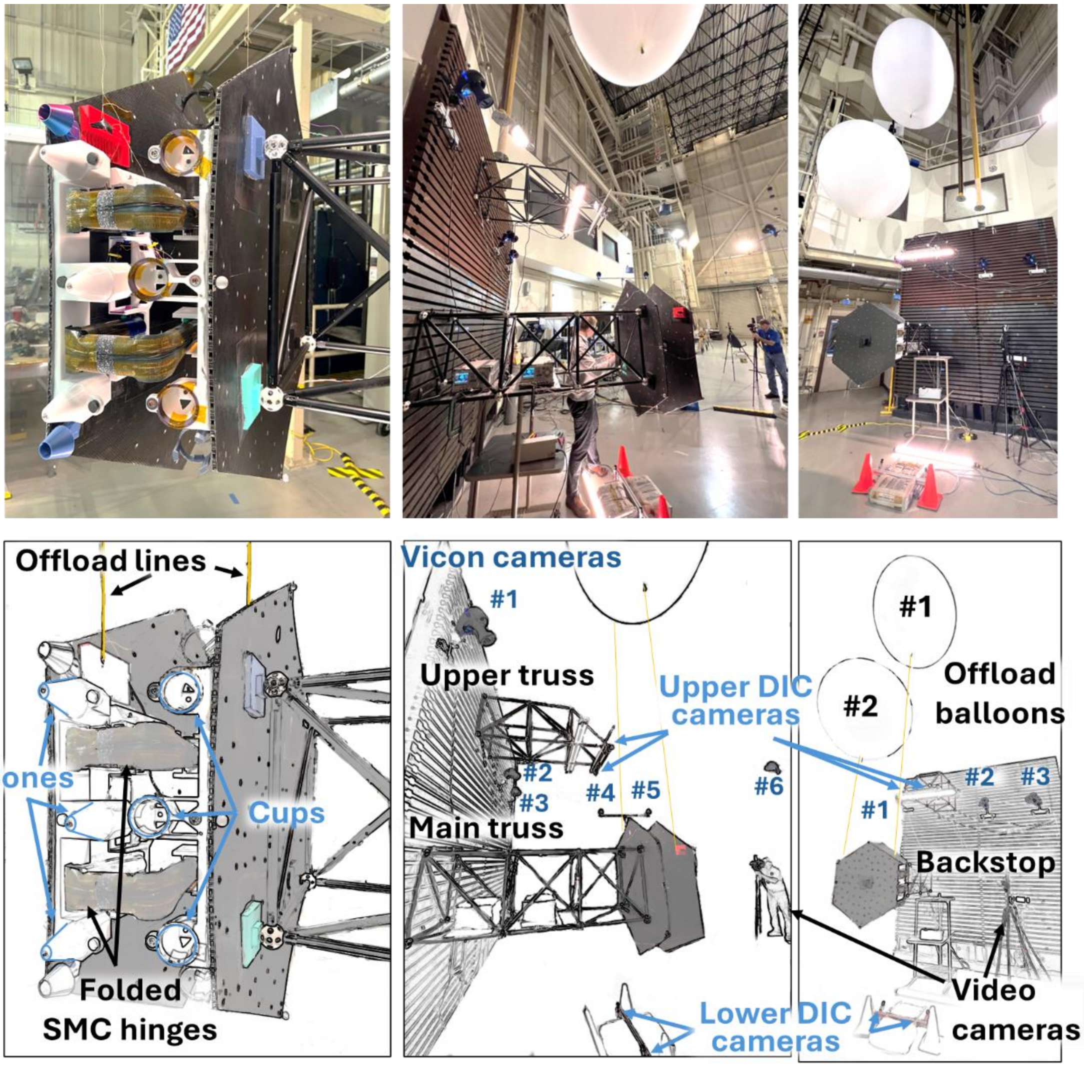

(a) (b) (c)

Fig. 22 Test setup for the final test campaign showing: (a) Test article in the stowed configuration with the fixed panel attached to the main truss and the moving panel attached to the fixed one via the two SMC hinges. Cup and cone features on the mating panel edges are shown. The moving panel is offloaded from two points; (b) Main and upper truss cantilevered from the backstop. Three power supplies for the hinge heaters and Frangibolt. Six Vicon cameras, lower and upper DIC camera pairs; (c) Offloading Helium-filled balloons attached to the moving panel. Video cameras.

Side panel balancing about the vertical axis was not needed as the tubular hinges deployed about that axis. To balance the panel about the remaining axis (symmetric axis of the panel) ballast mass was added to a cup bonded at the center of the panel at its concave side. Once the side panel was balanced, it was able to float from the two balloons in equilibrium. The balloons proved to be very effective for supporting the moving panel by offering minimal restraint to the test article in all degrees of freedom during panel deployment along the horizontal plane.

The same three power supplies used during the initial test campaign were used to provide adequate power to the heaters of each SMC hinge, and to actuate the NiTi Frangibolt release mechanism. There can see seen in Fig. 22(b), with two sitting on panels inside the main truss and one on a desk below.

D. Panel Deployment Tests

The stowed two-panel test article was fixed to the main truss cantilevered from the backstop wall. This provided a rigid connection to the fixed panel and allowed the moving panel to rotate about the fixed panel solely actuated by the composite tubular hinges, while being gravity offloaded by the two large Helium balloons. Four deployment tests were carried out during this final test campaign. Three tests used the SMC hinges for actuation to provide some repeatability metrics. A fourth test used equivalent non-SMC hinges that were energetically released to provide a direct comparison against the more self-dampened SMC hinge.

For the first three tests, to initiate the panel deployment process, the pairs of SMC hinges were brought up to their activation temperature above 125°C using the two power supplies. The SMC elements self-deployed, rotating the side panel off of the fixed panel. The Vicon videogrammetry system was used to track the motion of the targets attached to the fixed and moving panel, as well as the two balloon lines. The displacements on the x, y and z-axis of four of the retroreflective targets from the moving panel during Deployment Test #2 are displayed in Fig. 24, with the coordinate system represented in the top left diagram. The coordinate system had an origin on target #3 of the fixed panel, which was centered on the far edge of the panel. As shown in the Fig. 24 inset (upper left), the x-axis was along the symmetry line of the panel oriented in the initial direction of deployment, the y-axis was the vertical axis, and the z-axis was normal to both. The location of the six targets on the fixed panel are also shown in the top left diagram. The moving side panel had five targets (#1 through #5) arranged in a similar fashion to the fixed panel along the corners and far edge of the panel. The side panel took about 60 s to deploy.

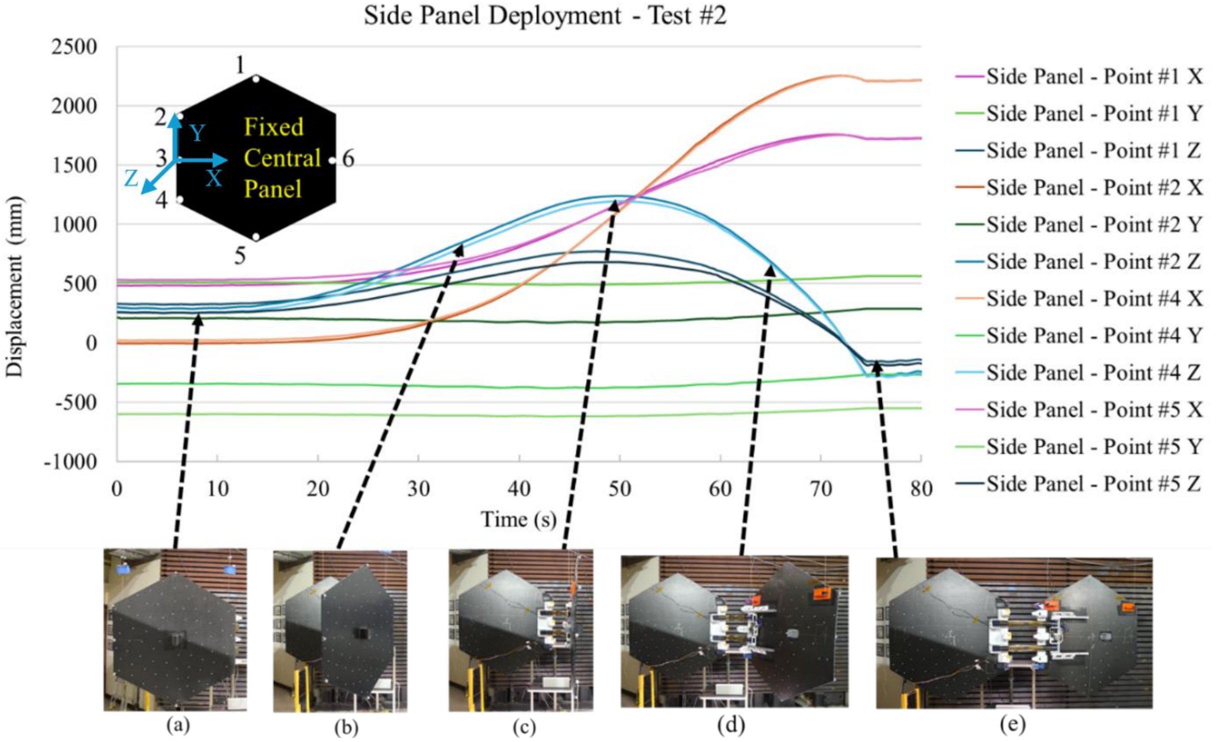

Fig. 24 Displacements of targets #1, #2, #4 and #5 during Panel Deployment Test #2. The top left diagram shows the location of the spherical targets on the moving panel, and the coordinate system, which has the origin on target #3 of the fixed panel. The X, Y, and Z displacements are represented in magenta/orange, green, and blue lines, respectively. The bottom images labelled (a) through (e) show the side panel at various stages of deployment, where the black dotted lines identify the points in the Z-axis displacement curve of one of the targets at the far edge of the side panel (#2 Z).

It can be observed that the X and Z motions of the opposite targets in the side panel, namely targets #1 and #5 (top and bottom corners of the panel), and targets #2 and #4 (top and bottom corners on the far edge) are very similar, resulting in a balanced planar motion over the deployment path. The relatively spiral motion of the side panel during Deployment Test #1 represented by its central far edge target #3 is depicted in Fig. 25. The planar displacements (X and Z) and radial distance from the fixed panel target #6 at the hinge line can be observed in Fig. 25 (a). Since the panel motion was mostly planar and spiral, a transformation of the reported data from cartesian to polar coordinates using as the reference point of origin the target #6 on the fixed panel and reference direction the Z axis, provided the radial distance and rotational angle of the panel about that point.

The radial distance of the far edge of the panel increased about 280 mm as expected due to the hinges recovering their original length. The rotational angle and angular speed of moving target #3 from fixed target #6 are presented in Fig. 25 (b). The rotational angle increased from -73° at the star of the test to +103° at the end for a total of 176°, slightly less than 180° due to the lack of a release mechanism for this test that precisely dictated the initial angle between the stowed panels. The panel over-rotated by 2.2° beyond the final configuration when the hinges locked straight due to the combined inertia of the panel and the large balloons before bouncing back.

The rotational rate smoothly varied over deployment with an average angular speed of 3.75 ± 1.5 °/s. There was a first phase of deployment that started at about 20 s into the test that ramped up the panel speed to a relatively steady ~5 °/s rate. When the panel had rotated about 90°, coincident with the maximum displacement in the Z axis, the far end of the slotted hinges snapped through producing the start of the angular rate spikes shown in Fig. 25 (b), which continued until the end due to the balloon dynamics. The end of deployment phase experienced rates dropping from +6.7°/s to -2°/s before settling to zero.

The average angular rates between the three panel deployment tests with the SMC hinges did not differ by more than 1.5°/s, providing similar graphs to the ones shown, as evidenced by Fig. 26 that presents the Deployment Test #2 results. The large spike in the angular rate graph corresponding to the far set of folded slots recovering occurred after the panel had rotated about 45°, much sooner than during Test #1. This timing also coincided with the one experienced during Test #3. Significant air drift was present in the test facility due to a working heating, ventilation, and air conditioning (HVAC) system, which was the cause of the low panel dynamics observed before the start of the test (first 20 s), and the longer duration of Test #2 and Test #3 over Test #1, when the HVAC unit was off. Moreover, the end of deployment of the last two tests experienced similar panel dynamics mainly due to residual balloon motion. The hinges recovered their original shape after panel deployment and rigidity after the heaters were turned off and the SMC material cooled down to room temperature. Upon close inspection, the two SMC hinges recovered without damage and they were reused for all tests.

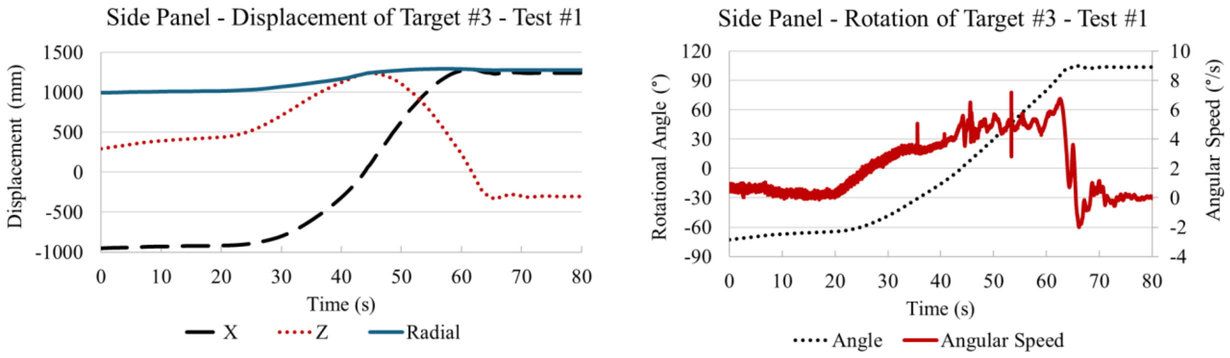

(a) (b)

Fig. 25 Spiral motion of the side panel during Deployment Test #1 represented by its far edge target #3: (a) Planar displacements (X and Z) and radial distance from the fixed panel target #6 at the hinge line; (b) rotational angle and angular speed of target #3 from fixed target #6.

For Test #4, the two-panel test article was retrofitted with another version of the tubular hinges. These hinges used the same composite material laminate as the prior set but did not have heaters attached and thus the shape memory effect of the material was not used. These units will be referred in the paper as non-SMC hinges. To reduce the likelihood of laminate failure and to reduce the strain energy in the stowed system, larger dogbone slots were cut on the non-SMC hinges. Both types of tubular hinges are shown in Fig. 27. The SMC hinges when programmed folded do not need any constraints, whereas the folded state of the non-SMC hinges needed to be restrained by 25-mm diameter tubing secured to the folded regions of the hinges by tape, as shown on the left images. Once the non-

SMC hinges were integrated into the test article, the tubing supports were removed and the two panels were secured into the deployment test began. The difference in size of the dogbone slot is evident in the recovered state of the tubes shown in the right images. While the dogbone slot design of the SMC hinges followed the nominal shape from Fig. 6, those of the non-SMC hinges had larger cutouts, with a slot length of 111 mm, a slot width of 15 mm, and an end slot hole diameter of 21 mm.

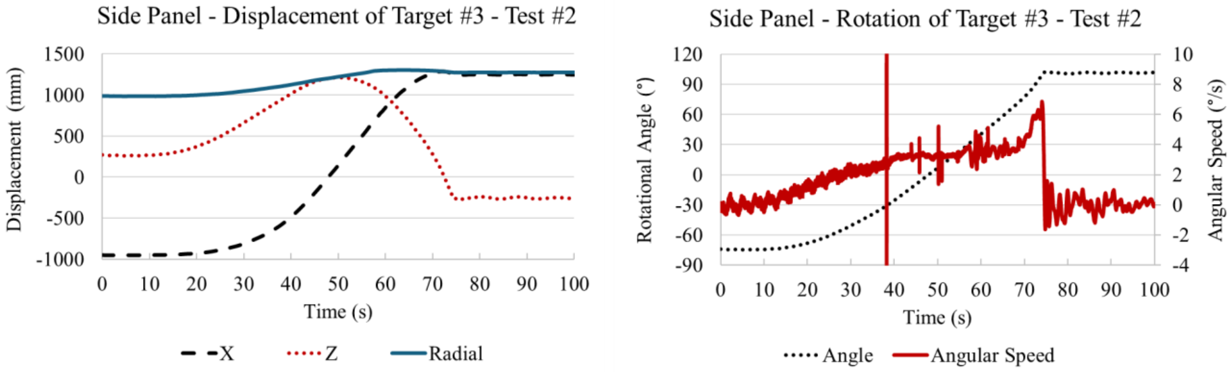

(a) (b)

Fig. 26 Spiral motion of the side panel during Deployment Test #2 represented by its far edge target #3: (a) Planar displacements (X and Z) and radial distance from the fixed panel target #6 at the hinge line; (b) rotational angle and angular speed of target #3 from fixed target #6.

The single panel deployment test with the non-SMC hinges attached produced a significantly faster deployment. While the panel deployed over 60-70 s during the three tests with the SMC hinges, the deployment time for the non-SMC hinges lasted 18 s, an over 3x time increased factor. The side panel deployment spiral path during Test #4 with the non-SMC hinges remained similar to the prior tests as shown in Fig. 28 (a). However, there were more induced dynamics in the system when the two folded regions of the slotted hinges straightened, as evidenced in the larger angular rates values presented in Fig. 28 (b). When the far end slots fully unfolded at a panel rotation of 48° the side panel reached an angular rate peak 21.1 °/s. When the slots closer to the fixed panel fully recovered the peak reached a rate of 26.5 °/s. The average angular rate during Test #4 was 9.7 ± 4.7 °/s, which was 2.5-4 times larger than those of the SMC hinge tests. The remaining vibrations after the end of deployment were also much larger than for the SMC hinge tests as shown on the right side of Fig. 26 (b) after the panel settles at a rotation angle of +103°. It is evident that a reflector design that used non-SMC hinges would need a secondary mean to dampen the deployment to reduce rates and final shock loads imparted to the spacecraft. Regardless of the more energetic and faster deployment, the two hinges recovered their nominal straight configuration without causing snap back at the end of panel rotation. Upon close inspection, the two hinges recovered without damage.

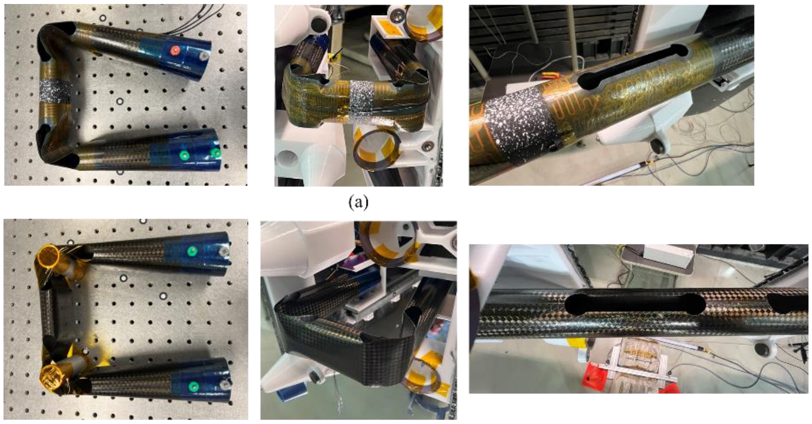

(a)

(b)

Fig. 27 Tubular composite hinges used for the tests: (a) SMC hinge; and (b) non-SMC hinge with a larger dogbone slots. From left to write the images show the programmed/folded state, the folded hinge integrated in the two-panel test article, and the recovered straight hinge after the panel deployment test.

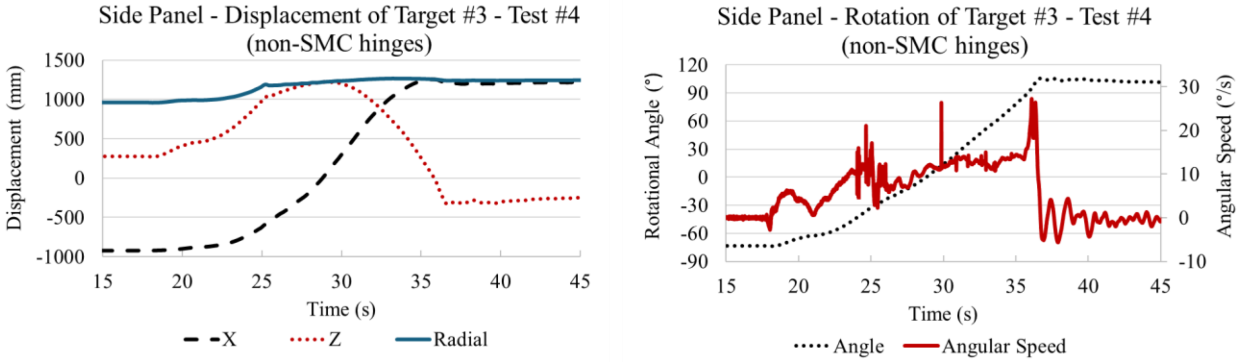

(a) (b)

Fig. 28 Spiral motion of the side panel during Deployment Test #4 represented by its far edge target #3: (a) Planar displacements (X and Z) and radial distance from the fixed panel target #6 at the hinge line; (b) rotational angle and angular speed of target #3 from fixed target #6.

E. Panel Latching Tests

The panel latching tests subsequently followed the panel deployment tests where two test configuration changes were needed. The first was to remove some of the ballast mass from the cup in the offloading line from the far end of the side panel. This change was needed to correct for the center of gravity of the side panel system shifting as the panel translated on its rails towards the fixed panel during the panel latching motion. A pre-test ballast mass removal of 190 g was used to artificially move the CG of the side panel mid-way through its expected translation, such that the panel would be balanced at that new location. Thus, during the first half of the motion, the cone elements of the panel mating edge would dip, and during the second half of the motion they would rise again meeting the cup elements. After the panels were latched, an additional 190 g of ballast mass were removed to balance the side panel in the final state before the final surface scan began.

The second test configuration change was to remove the previously used Frangibolt hardware that fixed the hinge end trolley on the rails to the side panel during the panel deployment phase. After several unsuccessful releases, the Frangibolt unit was removed for these series of tests. It is believed that the force exerted by the unit was causing deformation on the hinge trolley, which was 3D printed polycarbonate, such that the expansion of the NiTi shape memory alloy element of the Frangibolt was being absorbed by the plastic part rather than providing the tension needed to break the bolt. Therefore, the side panel was released by manually cutting a Kevlar string that was fixed to the anchor point of the lanyard reel spring on the one end, and a metal post outside of the test area on the other end. The string was arranged parallel to the extended lanyard reel it was pulling against to reduce moments.

The spring reel force was increased from the previously used 2-3 lbf to 4 lbf for these series of panel latching tests. The reason was that the large offloading Helium balloons had enough inertia to cause deceleration of the panel and also caused a pendulum motion in the side panel, which resulted in the lower corner of the mating edge arriving slightly before the upper corner. Upon making first contact and the bottom cone latching and providing some restoring moment opposite to that of the pendulum motion, the top corner hit and bounced back one time before latching assisted by the increased spring force. The same behavior repeated in all four latching tests following the Panel Deployment Test #1-4. For future tests, it is recommended to use much longer offloading lines to reduce their influence on the latching tests.

The relevant features of the latching test are shown in Fig. 29. The reflector backside hardware at the mating edges before and after the latching test are shown in Fig. 29 (a) and (b). The engaged cup/cone mating and latching elements at the bottom corner are shown in Fig. 29 (c). Fig. 29 (d) presents a close view of two of the V-groove and ball mounts from the cup/cone kinematic mount engaged. A global view of the two reflector panels latched can be seen in Fig. 29 (e). Finally, a close view of the mating edges on the concave reflective side of the panels is presented in Fig. 29 (f).

The X-axis displacement of target #3 of the side panel and the target on the far balloon string during Panel Latching Test #1 are shown in Fig. 30. The diagram on the right represents the test article including the coordinate axis, target locations on the panels and strings of the two offloading balloons. The panel travelled 260 mm in the -X direction in less than 0.5 s. There was rapid dynamic X-axis motion following the cup/cone engagement that dissipated after about 6-8 s followed by a very low amplitude cyclic motion. To explain the reason for this dynamic motion, the marker on the offloading far string is also plotted in Fig. 30 to reveal the sideways X-motion of the balloons. The observed lateral frequency of the string was about 0.25 Hz (4s period), which corresponds to the free motion of a pendulum in 1-g gravity with a 4 m line that is in line with the length of the string used on the far balloon. After this first test, a redesign of the latching approach was implemented by including two additional cup/cone elements at the mating end corners of the panels that better secured the original cup/cone kinematic mount, which was only relying on the magnets and lanyard reel spring force. The new cup/cone elements are shown in Fig. 29 (c) in blue/grey color. The cup side had three prongs that latched the cone part and prevented any backwards motion.

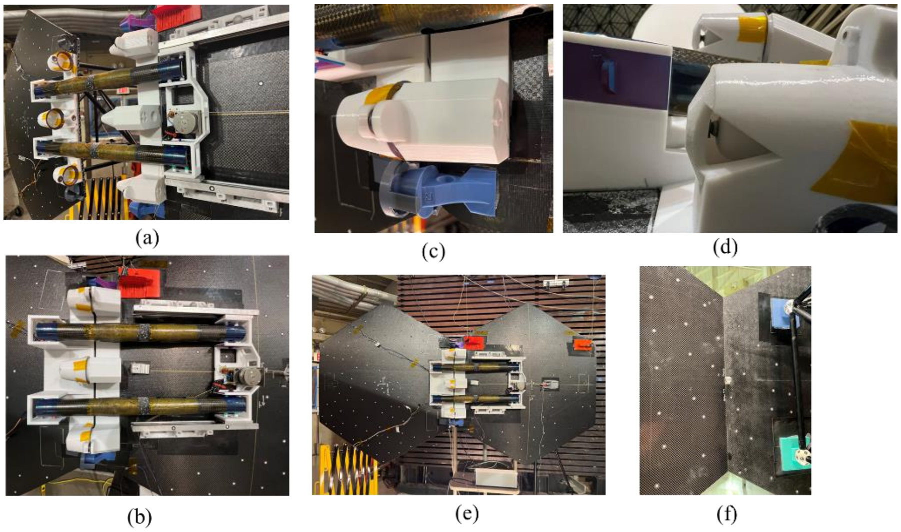
(a) (c) (d)
(b) (e) (f)

Fig. 29 Relevant features of the latching test: (a) Reflector backside hardware at the mating edges before the latching test; (b) mating edges after the latching test; (c) engaged cup and cone mating and latching elements; (d) close view showing two of V-groove and ball mounts from the cup/cone kinematic mount engaged; (e) global view of the two reflector panels latched; (f) close view of the mating edges on the concave reflective side of the panels.

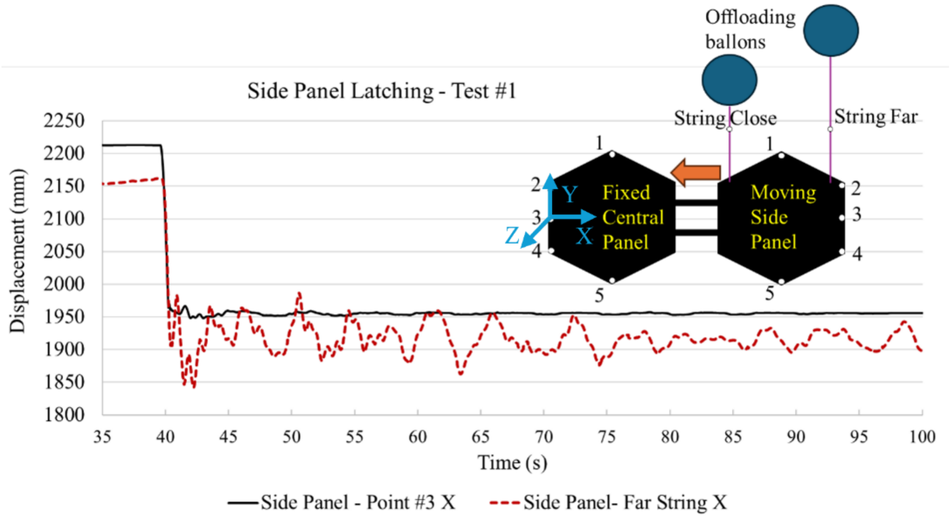

Fig. 30 X-axis displacements of target #3 of the side panel and the target on the far balloon string during Panel Latching Test #1. Given the residual motion of the panel after panel latching due to the balloon dynamics above the test article an improved latching mechanism was implemented in subsequent tests. The diagram on the right represents the test article including the coordinate axis, target locations on the panels and strings of the two offloading balloons.

The displacements of target #3 located at the center of the far edge of the moving panel during Panel Latching Test #2 after implementing the new latches are shown in Fig. 31 for two time windows from the start of the test. The diagram on the right represents the new coordinate axis centered on target #3 of the moving panel used to represent the data, which is why at the start of the test all displacements are zeroed. The 10-s span graph Fig. 31 (a) shows that only residual motion after panel latching is present in the Z-axis, which is the normal axis to the panel assembly that is the most flexible out-of-plane axis of the joint. Offload balloon dynamics are still present for some time while the balloons come to a rest. The 2-s span graph of Fig. 31 (b) reveals details of the panel close-out motion. The cones elements enter the cups 0.4 s into the test and the final kinematically locked position is reached 1.2 s into the test. In between, the majority of the motion at the far edge of the panel occurs normal to the x-axis. The dipping/rising of the panel along the vertical y-axis is evident, and so is the out-of-plane motion along the z-axis. The in-plane motion of the panel is perfectly locked once the added latches are fully engaged.

To showcase the pendulum motion and bounce-back of the panel, the in-plane motion of the targets #1 and #5 attached to the top and bottom corners of the side panel during Panel Latching Test #2 are presented in Fig. 32. The X-axis data from Fig. 32 (a) shows the panel was initially tilted counterclockwise about the Z axis with a ~25 mm offset between the two opposite corners due the ballast removal on the far edge of the panel. As panel motion progressed, the bottom corner rotated clockwise and the panel cones entered the receiving cups at the same time at about 0.4 s into the test. At this moment, the bottom latch engaged first and target #5 remained fixed. However, the top mating edge of the panel bounced back inside the top cup/cone element from the shock load until the top latch fully engaged at 1.2 s into the test. The much smaller scale of the Y-axis data from Fig. 32 (b) indicates that not much vertical motion occurred during the panel latching tests. The only difference of a couple of millimeters between the top and bottom corners data while the panel was translating, which is related to the aforementioned clockwise motion. Once the first latch engaged, the vertical motion is the result of play in the cup and cone interfaces before the top corner latch engaged.

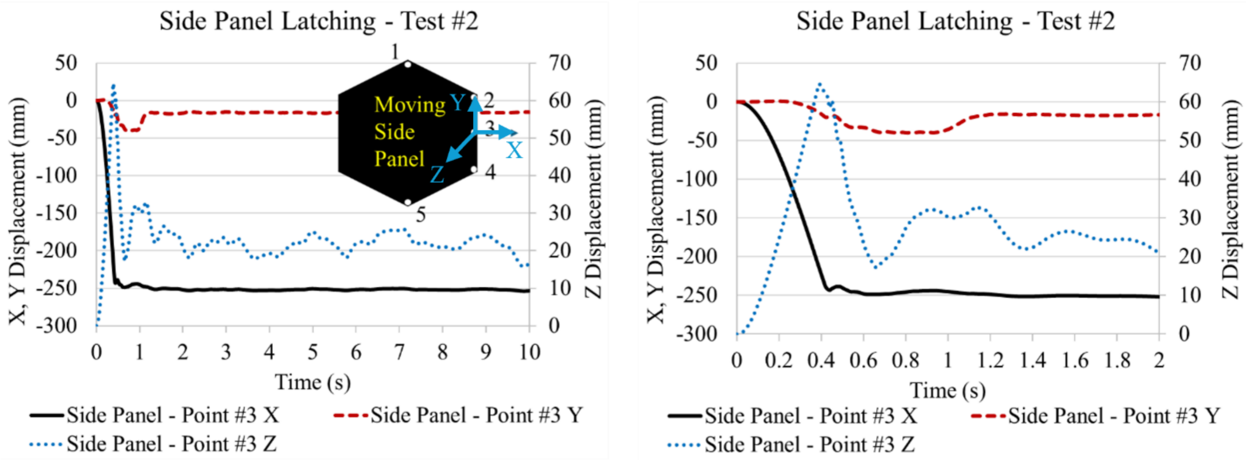

(a) (b)

Fig. 31 Displacements of target #3 of the side panel during Panel Latching Test #2: (a) First 10 s of the test; (b) Zoom in of the first 2 s of the test. For clarity the X, and Y values are on the left ordinate axis of the graph and the Z values are on the right ordinate axis. The diagram on the left figure represents the new coordinate axis centered on target #3 at the far edge of the moving panel.

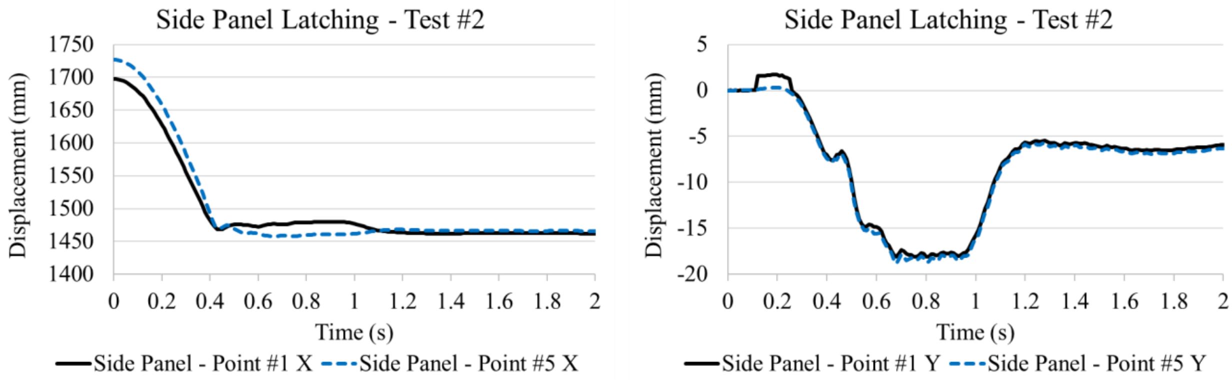

(a) (b)

Fig. 32 Displacements of target #1 (top corner) and #5 (bottom corner) of the side panel during Panel Latching Test #2: (a) X-axis displacements; (b) Y-axis displacements.

F. Deployed Surface Metrology Results

After every latching test, the 3D handheld scanner previously described was utilized to scan the concave surface of the mated panel assembly. These measurements are referred to as the post-test scans. The post-test scans were then compared to:

1) The final panel alignment scan, known as the pre-test scan shown in Fig. 20 (b) to provide the test error.
2) The reference assembly scan performed using the as-manufactured panel scans that were mated in the metrology software to provide the best fit against the nominal CAD model of the two-panel assembly. This comparison provided the total error not including manufacturing error. The deviation of this reference assembly surface against the nominal assembly geometry is shown in Fig. 33 (a) and is considered the best alignment possible given panel imperfection.
3) The nominal CAD model of the assembly to provide the total error.

To perform the final scans, the retroreflective spheres for Vicon were replaced with the matte black spheres used as the alignment datums for the scan comparisons. Both spheres shared the same base attachment to the panel so their location did not change. Scans were not performed until the offloading balloons were at a stop. As mentioned, 190 g of ballast mast was removed for the far end offloading line to better balance the side panel in the final latched configuration though it is believed to not have a real effect on the surface shape after the panels were latched, as evidenced by the in-plane (X-Y) displacement data of Fig. 31 and Fig. 32.

The comparison between the post-test scan from the end of Test #1 and the pre-test scan taken at the end of the panel alignment process previously shown in Fig. 20 is presented in Fig. 33 (b). The relatively large deviation of the side panel at the mating end, which remains less than ±1 mm, is due to small rotation across the relatively flexible cup/cone joint prior to adding the latching elements. Note that the much larger 7 mm deviation at the far end of the 1 m wide panel translates to a 0.4° angle at the joint line. There was residual Z-axis motion in the panel due to the air drift disturbance in the facility moving the offloading balloons, which were still needed to maintain alignment of the joint line. Due to this effect, up to ±2 mm deflection at the far end of the panel was measured several minutes after the latching tests, partially smearing the scan measurements. This deflection reduced to less than ±0.5 mm once the latching mechanism was implemented, but it was still present.

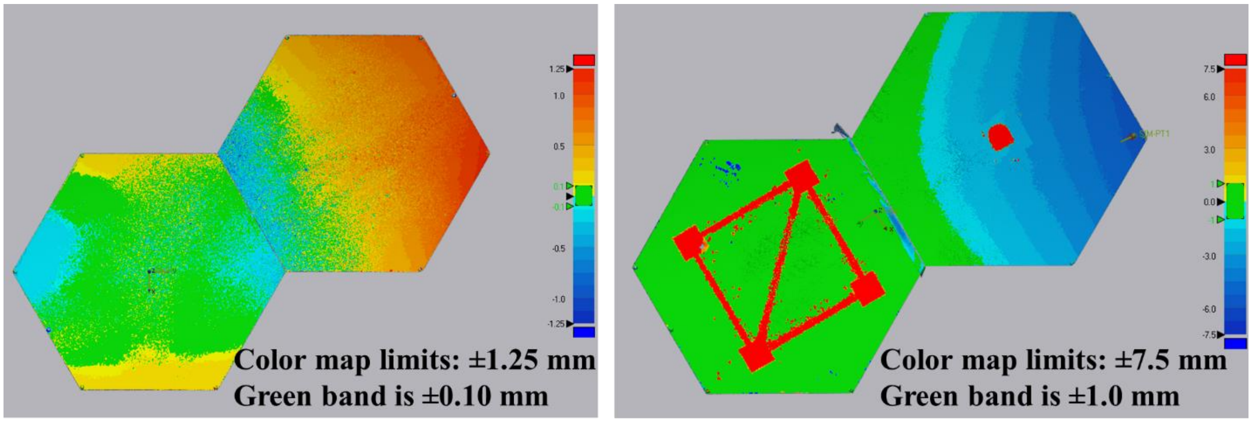

(a) (b)

Fig. 33 Surface comparison deviation contour plots between: (a) best-fit reference panel assembly alignment against the nominal CAD panel assembly model geometry. This is considered the best alignment possible given panel manufacturing error; (b) Post-test scan from the end of Test #1 against the pre-test scan. The red and blue indicate where the comparison surface is above (out of the page) or below from the reference surface. In both images the left and right panels are the central and side panel, respectively. The left and right plots have ±1.25 mm and ±7.5 mm deviation limits. The square red elements shown at the central and side panels of the right image are the end of the support truss and the ballast cup holder for balancing.

The comparison of surface deviation contour plots between the end of Test #2 and the pre-test scan, known as the functional test error, is shown in Fig. 34 (a). The deviation contour plot of the side panel appears opposite to the final alignment pre-test scan shown in Fig. 20 (b), where the top corner of panel was low and the bottom corner at the far edge was high. The calculated test RMSE of the side panel during Test #2 is 0.916 mm. The comparison between the Test #2 scan deviation plot and the nominal CAD model geometry, also known as the total error, is presented in

Fig. 34 (b). The calculated total RMSE of the side panel during Test #2 is 0.794 mm. Both plots have ±1.0 mm deviation limits. The green color band shown in those figures presents an order of magnitude lower limits than the global ones The cup and cone panel latching elements used in Test #2 reduced the surface deviation significantly. However, it is believed that the majority of the error towards the far end of the panel is from air disturbance. The lingering Z-axis motion of the panel was presented in Fig. 31 (a), and although the permanent oscillation amplitudes dropped an order of magnitude from those shown, they were large enough to decrease the accuracy of the post-test scans. The accuracy of the Test#2 results would reflect a deployed reflector surface that would be in line with the needs of X-band RF transmission antennas.

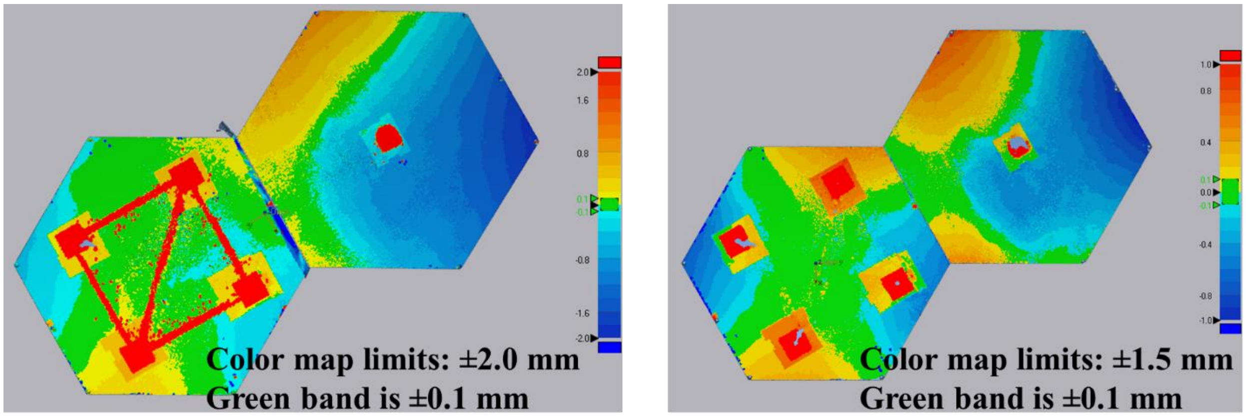

(a) (b)

Fig. 34 Surface comparison deviation contour plots between the end of Test #2 and: (a) the final alignment pre-test scan, also known as the functional test error; (b) the nominal CAD model geometry, also known as the total error. The left and right plots have ±2.0 mm and ±1.0 mm deviation limits. The green band on both plots have ±0.1 mm deviation limits. The red and blue indicate where the comparison surface is above (out of the page) or below from the reference surface.

Calculating accurate RMSE values for both the combined side and central panels for these scan comparisons was not possible due to the truss support items attached to the central panel skewing the results. Therefore, only the side panel RMSE values will be presented, which are the relevant ones for the testing phase. The side panel surface deviation RMSE values are shown in Table 1. In general, it was observed that the local deviation near the side panel mating edge was very low (less than 0.2 mm RMSE) giving confidence to the design of the alignment and latching features. The relatively large deviations in Test #1 were a result of the air drift disturbance and the lack of an adequate latching feature. Subsequent tests #2 and #3 with latches reduced the error significantly, producing total RMS errors under 0.8 mm. A repeat of Test#2, where the side panel was disengaged and the test was repeated produced two times larger errors. The result with the non-SMC hinges (Test #4) produced similar errors to the repeated test, which probably indicates that the resolution of the measurements given the air drift is of the order of the error. In summary, the metrology scans revealed that the new reflector architecture is promising towards achieving the surface accuracy required by X-band communication systems that allows up to 1 mm RMSE.

Table 1. Side panel surface deviation RMSE.

Test	Functional test error (mm)	Total error from reference alignment (mm)	Total error (mm)
#1 (before latches)	2.671	2.352	2.473
#2	0.916	0.567	0.794
#2b (repeat)	1.717	1.259	1.488
#3	0.979	0.732	0.745
#4 (non-SMC hinges)	1.503	1.536	1.504

VII. Conclusions and Outlook

A new architecture for deployable solid surface segmented reflector antennas using a vertically stacked arrangement of the rigid panels enabled by shape memory tubular hinges was presented. The reflector design is compatible with robotic assembly methods to create larger versions in space.

An initial breadboard testing campaign revealed design deficiencies and provided lessons learned for testing in gravity. A final test campaign with a brassboard model of a two-panel reflector assembly provided promising results in terms of stowage behavior, deployment dynamics and repeatability, test approach with gravity off-loading, and final deployed surface accuracy. The fabrication of the novel hinges and reflector panel components was an iterative process. The final units for both are close to space-rated versions.

Finite element analysis was used as a design tool for the tubular hinges and end fixation boundary conditions to provide stowage without damage and final recovery without bounce back. Both active SMC and passive non-SMC versions of the hinges were successfully fabricated and tested. Major differences in the hinge stowed and deployment behavior was observed. The non-SMC hinges required additional support in the folded state, which stowed significantly more strain energy than the SMC version and deployed in one third of the time. The SMC hinges proved to deliver more controlled panel deployment with fewer dynamics and reduced final shock load. For a flight system, a non-SMC hinge of this type would need an damper system to reduce its rates.

Advanced non-contact measurement systems were effectively used to track the motion of the test article and the ground support equipment (Vicon videogrammetry), the full-field displacements, strains and curvatures of segments of the hinges (VIC 3D DIC photogrammetry), and to measure the surface of the reflector test article and for comparison with reference measurements or the nominal model (3D handheld scanner and Geomagic metrology). Since similar target features attached to the test article were used for all measurement systems it is possible to use part of the data from one system for validation of the data from other systems.

The configuration of the panel deployment tests were changed from the rotation axis of the hinges being normal to gravity (vertical configuration) to being parallel to gravity (horizontal configuration) reducing gravity-induced moments on the test article. The gravity off-loading system was simplified from the first version using a U-frame that enabled rotation of the panel about its axis that translated on an overhead track with the pulley system holding the offloading mass, to the final version using a pair of helium-filled balloons that freed all degrees of freedom of the moving panel. The latter approach proved successful at minimizing its influence on the panel deployment phase, since the angular rates were small. However, for the panel latching phase that was not a quasi-static event, the balloons introduced parasitic inertial forces both during the panel travel (pendulum motion) and at the end (residual vibrations). Lower amplitude vibrations of up to ±2 mm were initially measured at the far end of the side panel, which significantly smeared the final surface scan measurements. However, after an improved latching mechanism was implemented, the magnitude of these vibrations reduced to less than ±0.5 mm, which provided cleaner surface scans. A comparison of the deployed reflector surface deviation between the measured surface after the stowage and deployment process and the pre-test scans and the nominal surface revealed root mean square errors of less than 1 mm. This accuracy is required by X-band and above radiofrequency transmissions for space antenna applications. With further improvements in panel fabrication and assembly, and testing refinement, surface accuracies with RMSE of less than 0.3 mm, as required by Ka-Band and above RF transmissions, are achievable.

Following these series of tests, the reflector concept and its key components are arguably at TRL 4. A similar test campaign with the complete seven-panel reflector is planned. For these future tests, it would be advantageous to also characterize the acceleration imparted by the lanyard reel spring used to mate the panels by using an accelerometer mounted on the fixed panel. RF performance and environmental testing on a similar version of the test article but where the 3D printed plastic parts are replaced by metal counterparts would be needed to raise the TRL to 5.

Acknowledgments

This research was funded by the NASA Space Technology Mission Directorate (STMD) under an Announcement of Collaboration Opportunity (ACO) project called Advanced Packaging Reflector Methods (APRM) in partnership with Maxar Technologies, and subsequent NASA LaRC internal research and development funding. Mechanical designs were partially produced and analyzed by Kevin Demarco and Kevin Roscoe, and the testing support from Matthew Stasolla, Jose Morel and Jay Warren is gratefully acknowledged. Jin Ho Kang developed the shape memory polymer resin. Fabrication expertise from Kevin McLain, Phillip Tofts, David Tucker and Kade Kunkel was also instrumental to this effort.

References

[1]M. M. Mikulas Jr., P. R. Withnell, “Construction concepts for precision segmented reflectors,” AIAA Paper 93-1461, 1993.

[2]B. B. Allen, C. F. Willer, R. I. Harless, R. V. Valentin, R. S. Sorrell, “Compactly stowable thin continuous surface-based antenna having radial and perimeter stiffeners that deploy and maintain antenna surface in prescribed surface geometry,” U.S. Patent 6,344,835 B1, Issued 5 February 2002.

[3] J. Footdale, J. Cody Griffe, M. E. Peterson, and C. Box, "Flexible composite shell design for the MARCO deployable reflector," *AIAA Scitech 2019 Forum*, 7-11 January 2019, San Diego, CA.

[4] M. M. Mikulas Jr., T. J. Collins, J. M. Hedgepeth, "Preliminary design approach for large high precision segmented reflectors," NASA Technical Memorandum 102605, 1990.

[5] J. Sauder, N. Chahat, J. Mejia-Ariza, S. Prasad, G. Hanes, J. Byars, T. Rogenmoser, S. Brown, R. Rodriguez-Monje, "Starburst: a concept for a new deployable structure architecture," AIAA Scitech 2024 Forum, 8-12 January 2024, Orlando, FL.

[6] Y. She, S. Li, Z. Wang, "Constructing a large antenna reflector via spacecraft formation flying and reconfiguration control," *AIAA Journal of Guidance, Control, and Dynamics*, Vol. 42, No. 6, June 2019.

[7] NASA, *https://www.nasa.gov/press-release/nasa-funds-demonstration-of-assembly-and-manufacturing-in-space*, published Jan. 31, 2020.

[8] J. M. Fernandez, J. H. Kang, "Shape memory polymer composite substrate," U.S. Patent Application 18/605,929 filed on March 17, 2023.

[9] J. M. Fernandez, A. F. Paddock, K. Demarco, "Composite substrate reflector design," U.S. Patent Application 18/606,423 filed on March 17, 2023.

[10] J. M. Fernandez, A. F. Paddock, K. O'Neal, K. Demarco, "Segmented hexagonal antenna reflector concentrically stacked using shape memory composite tubular hinges", 41st ESA Antenna Workshop, 25-28 September 2023, ESA/ESTEC, Noordwijk, The Netherlands.

[11] H. M. Y. C. Mallikarachchi, S. Pellegrino, "Optimized design of composite booms with integrated tape-spring hinges," AIAA 2010-2750.

[12] D. S. Adams, M. Mobrem, "Lenticular jointed antenna deployment anomaly and resolution onboard the Mars Express spacecraft," AIAA Journal of Spacecraft and Rockets, Vol. 46, No. 2, pp. 403-410, March-April 2009.

[13] Yao, Y., Taylor, J., Cirullo, L., Leguarda, R., Sheeran, B., Ning, X., "Ultra-thin, ultra-lightweight, and multifunctional skin for highly deformable structures," *AIAA Scitech 2019 Forum*, 7-11 January 2019, San Diego, CA.

[14] J. M. Fernandez, A. F. Paddock, K. P. Roscoe, K. Demarco, "Segmented, pleat-folded and rib-supported thin-shell composite antenna reflector," 41st ESA Antenna Workshop, 25-28 September 2023, ESA/ESTEC, Noordwijk, The Netherlands.